

Light Water Reactor Sustainability Program

Thermodynamic and kinetic model of phase stability in austenitic steel under light water reactor conditions



August 31, 2018

U.S. Department of Energy
Office of Nuclear Energy

DISCLAIMER

This information was prepared as an account of work sponsored by an agency of the U.S. Government. Neither the U.S. Government nor any agency thereof, nor any of their employees, makes any warranty, expressed or implied, or assumes any legal liability or responsibility for the accuracy, completeness, or usefulness, of any information, apparatus, product, or process disclosed, or represents that its use would not infringe privately owned rights. References herein to any specific commercial product, process, or service by trade name, trade mark, manufacturer, or otherwise, does not necessarily constitute or imply its endorsement, recommendation, or favoring by the U.S. Government or any agency thereof. The views and opinions of authors expressed herein do not necessarily state or reflect those of the U.S. Government or any agency thereof.

Light Water Reactor Sustainability Program

Thermodynamic and kinetic model of phase stability in austenitic steel under light water reactor conditions August 31, 2018 Milestone

**Shipeng Shu (University of Wisconsin–Madison)
Mahmood Mamivand (University of Wisconsin–Madison)
Huibin Ke (University of Wisconsin–Madison)
Tam Mayeshiba (University of Wisconsin–Madison)
Benjamin Afflerbach (University of Wisconsin–Madison)
Jia-Hong Ke (University of Wisconsin–Madison)
Dane D. Morgan (University of Wisconsin–Madison)**

Key Collaborators

**G. Robert Odette (University of California, Santa Barbara)
Peter B. Wells (University of California, Santa Barbara)
Nathan Almirall (University of California, Santa Barbara)**

August 31, 2018

**Prepared for the
U.S. Department of Energy
Office of Nuclear Energy**

SUMMARY

This report has been assembled to address the following milestone due August 31, 2018:

Milestone Number: M2LW-18OR0402053

Title: “Complete report on the thermodynamic and kinetic model of phase stability in austenitic steel under light water reactor conditions”

ACKNOWLEDGEMENTS

This research was sponsored by the United States Department of Energy, Office of Nuclear Energy, for the Light Water Reactor Sustainability Research and Development effort.

CONTENTS

SUMMARY	iv
ACKNOWLEDGEMENTS	v
ACRONYMS AND NOMENCLATURE	xii
1. INTRODUCTION	1
2. EXECUTIVE SUMMARY OF MAJOR RESULTS	3
3. METHODS	4
3.1 Cluster Dynamics Simulations	4
3.1.1 Basic Cluster Dynamics model.....	4
3.1.2 Simulation Models for carbide precipitation in Austenitic stainless steels	6
3.1.3 Simulation Models for the ferritic low-alloy RPV steels	10
3.1.4 Parameters for the MNSP Cluster Dynamics model	13
3.1.5 Parameters for the Cu-MNS Precipitates Cluster Dynamics model.....	16
3.2 Machine Learning.....	18
3.2.1 Introduction	18
3.2.2 Model introduction.....	19
3.2.3 Model fitting method – cross validation.....	20
3.2.4 Model details	21
3.3 Experimental	21
3.3.1 Materials and irradiation conditions.....	22
3.3.2 Atom probe tomography	23
4. RESULTS	26
4.1 Cluster Dynamics	26
4.1.1 Precipitation of Carbides in 316 stainless steels: without irradiation.....	26
4.1.2 Precipitation of Carbides in 316 stainless steels: effect of irradiation	28
4.1.3 Precipitation of Carbides in 316 stainless steels: effect of change of solute product.....	34
4.1.4 Precipitation of Cu-MNS in RPV steels.....	35
4.2 Machine Learning.....	39
4.2.1 Results.....	39
4.3 Precipitation in Fe-Cu and Fe-Cu-Mn alloys	42
4.3.1 APT analysis.....	42
4.3.2 Comparing results from ion irradiations and those from neutron irradiations.....	47
4.3.3 Discussions.....	50
5. SUMMARY OF MAJOR RESULTS.....	59
5.1 Cluster Dynamics	59
5.1.1 Cluster dynamics simulation of carbide precipitation in 316 stainless steel	59
5.1.2 Cluster dynamics simulation of Cu bearing ferritic RPV steels	59
5.2 Machine Learning.....	59
5.3 Precipitation in Fe-Cu and Fe-Cu-Mn alloys: dose rate effect.....	60

6.	FUTURE WORK	61
----	-------------------	----

FIGURES

Figure 1. Temperature dependence of the carbide composition. (a) $M_{23}C_6$; (b) M_6C	7
Figure 2. Equilibrium solute product of the carbides.	7
Figure 3. A flowchart of precipitate formation in RPVs in the presence of Cu.	18
Figure 4 The ion irradiation dose and dose rate as a function of depth below the sample surface, for both Fe-Cu and Fe-Cu-Mn samples. The low-dose sample was used for the 0.03 dpa APT tips; the high-dose sample was used for the 0.3 dpa, 1.1 dpa and 3.0 dpa APT tips.....	23
Figure 5 Evolution of total carbides ($M_{23}C_6$ and M_6C) volume fraction compared to experimental data. We note that the nature of precipitates in Renault (2009) were uncertain and could be carbide or G-phase. Adapted from Ref. [4].....	27
Figure 6. CD simulation of annealing of a 316 SS at 320 °C (a) volume fraction (b) precipitate radius (c) precipitate number density.....	28
Figure 8. Precipitate evolution at 1 dpa (a) volume fraction (b) precipitate radius (c) precipitate number density.....	32
Figure 9. Precipitate evolution as a function of irradiation dose.	33
Figure 10. volume fraction of $M_{23}C_6$ at 10 dpa, plotted as a function of solute product increase.	35
Figure 11. Comparison between CD model and experimental results for evolution of precipitates in LC, LD, LH, and LI alloys as a function of fluence. Yellow line is the CD results for an average irradiation condition (1×10^{16} n/m ² /s, 290 °C) obtained using the SANS fitting process. Green triangles denoted CD points that are values calculated at the exact conditions of the experiments.....	37
Figure 12. A detailed examination of volume fraction of different phases nucleated by various mechanisms of LC (modeled as $Cu_{0.25}Ni_{0.81}Mn_{1.1}Si_{0.46}$) alloy irradiated at a flux of 1×10^{16} n m ⁻² s ⁻¹ . The results show that at very high fluence, the volume fraction of appendage precipitates decreases, in favor of MnNiSi precipitates on dislocations.	38

Figure 13. (a) Full fitting and (b) 5-fold cross-validation (CV) of IVAR+ experimental data using the GKRR model. The best and worst CV fits are evaluated out of 100 cross-validation tests. For each cross-validation test, the RMSE values from each of the five folds are averaged into a single RMSE value. The best CV fit has the lowest fold-average RMSE of the 100 tests, and the worst CV fit has the highest fold-average RMSE. The points shown in red or blue are for all five folds of each test.	39
Figure 14. Heatmap of GKRR model performance across a wide range of hyperparameters. Orange boxes identify a region of degenerate performance in the hyperparameters don't significantly change the performance of the 5-fold cross validation test.	40
Figure 15. RMSE of predicting ATR2 dataset with 8 different hyperparameter combinations identified from the IVAR+ CV testing.....	41
Figure 16. Gaussian Process Model prediction of the ATR2 dataset	42
Figure 17: 20 nm thick sections from atom maps showing species distribution for Fe-Cu alloys irradiated at different doses. (a) 0.03 dpa (b) 0.3 dpa (c) 1.1 dpa (d) 3.0 dpa. Cu atoms are shown in green. Only solute atoms are shown. Note the background signal is not corrected by IVAS in the visualization of the reconstruction, which leads to higher apparent Cu composition in the matrix in some cases (for instance in the 0.3 dpa sample).	43
Figure 18: 20 nm thick sections from atom maps showing species distribution for Fe-Cu-Mn alloys irradiated at different doses. (a) 0.03 dpa (b) 0.3 dpa (c) 1.1 dpa (d) 3.0 dpa. Cu atoms are shown in green, and Mn atoms are shown in blue. Only solute atoms are shown.	45
Figure 19: Precipitate size distribution. (a) Fe-Cu (b) Fe-Cu-Mn	46
Figure 20: Cu composition in precipitates in Fe-Cu-Mn alloy as a function of irradiation dose.	47
Figure 21: Radial Mn concentration profile plotted as a function of distance from Cu/Fe interface in the Fe-Cu-Mn alloy. The profiles are not corrected for Fe in the precipitates, although this Fe content is likely an artifact of the APT method.	47

Figure 22: The precipitate volume fraction, diameter and number density of precipitates for both the Fe-Cu and Fe-Cu-Mn alloys, plotted as a function of irradiation dose.	50
Figure 23: Precipitation size plotted as a function of effective dose (dpa), which considers the dose rate effect on RED. (a) Fe-Cu; (b) Fe-Cu-Mn.	53
Figure 24: (a) Radiation enhanced Cu diffusion coefficient as a function of dose rate and the equivalent flux. Five diffusion regimes are denoted for the Fe-Cu alloy. (b) gamma as a function of dose rate and the equivalent flux.....	58

TABLES

Table 1 Chemical composition of typical 316 stainless steel.	6
Table 2 Thermal diffusion coefficients of carbide components in 316 SS at 320 °C [4].	9
Table 3 Equilibrium solute product for each phase at different temperatures	14
Table 4 Diffusion coefficients under thermal condition.....	15
Table 5 Parameters used in calculating radiation enhanced diffusion coefficient and other parameters.....	15
Table 6 Summary of fluxes and fluences of neutron irradiation.	23
Table 7. Summary of the microstructural measurements by APT for Fe-Cu alloy	43
Table 8 Summary of the microstructural measurements by APT for Fe-Cu-Mn alloy	45

ACRONYMS AND NOMENCLATURE

APT	Atom probe tomography
BCC	Body-centered cubic
CD	Cluster dynamics
CM6	Name of different alloy composition used by University of California, Santa Barbara, collaborators
CRP	Cu-rich precipitate
CV	Cross Validation
GKRR	Gaussian Kernel Ridge Regression
LC, LD, LH, LI, LG	Name of different alloy composition used by University of California, Santa Barbara, collaborators
LO	Leave-out
LWR	Light water reactor
KMC	Kinetic Monte Carlo
MNSP	Mn-Ni-Si rich precipitate
PIA	Post-irradiation annealing
RIS	Radiation-induced segregation
RMSD	Root mean square difference
RMSE	Root mean square error
RPV	Reactor pressure vessel
SS	Stainless steel
UMD	Unstable matrix defects

1. INTRODUCTION

Both Austenitic stainless steels and low-alloy ferritic steels find broad applications in the nuclear industry. Austenitic stainless steels are major structural materials in the nuclear reactor core, thanks to their high strength, corrosion resistance, and formability. However, in the harsh environment of the reactor core, elevated temperature and neutron irradiation lead to materials degradation, including void swelling and precipitation hardening. Specifically, precipitation in the 316 austenitic stainless steels has been studied in a number of irradiation conditions [1-3]. Experimental studies have revealed that the following precipitates can form at temperatures below 400 °C: $M_{23}C_6$ and M_6C carbides, γ' (Ni_3Si) and G-phase ($M_6Ni_{16}Si_7$). In this milestone report, we focus on carbide precipitation under irradiation. The main motivation is that, in experiments, the observed volume fraction of carbide appears to be smaller than the thermodynamic prediction [1-4]. We study the effect of irradiation dose rate on the stability of the carbides, with a goal to help better understand the experimental studies. Specifically, we assess the possible competition between radiation enhanced diffusion and ballistic mixing, and assess if the latter might be a source of reduced carbide volume fraction. To achieve the goal, we developed a cluster dynamics (CD) model which treats the combined effects of radiation enhanced diffusion and ballistic dissolution. The model was used to gain insights regarding the precipitation evolution mechanisms of the carbide precipitates.

Although the work during this milestone period has focused on austenitic alloys, we have also maintained a small effort related to reactor pressure vessel (RPV) steels that was needed to complete work from the previous milestone period. Therefore, we also report on these efforts and summarize them below.

One of the projects is on the hardening of RPV steels. Made primarily by ferritic low-alloy steels, RPVs are permanent components in light water reactors (LWRs) and their irradiation embrittlement is one of the potential barriers to extending the lifetime of light water reactors. Therefore, predicting and having insight into the RPVs embrittlement in extended life conditions play a critical role in LWRs further licensing. In this report, we have made further progress on ongoing projects that use cluster dynamics models to study the RPVs embrittlement and gain insight into extended life conditions. New observations and discussions are reported. The details of the cluster dynamics method for this system are included for completeness. We have also developed a machine-learning-based approach, as opposed to a physics-based approach, to

modeling the mechanical response of RPVs. Here we report on recent developments in our machine learning model and its performance for fitting and predicting changes in RPV yield stress.

The other RPV related work that we include in this report is on the irradiation dose rate effect of Cu precipitation in ferritic alloys. Specifically, to reduce the complexity of studying multi-solute RPV alloys, we use two model alloys: Fe-Cu and Fe-Cu-Mn. Irradiation dose rate effects are studied using accelerated-damage experiments in test reactors and charged-particle accelerator facilities. Neutrons and ions create vacancy and self-interstitial defects, whose production is measured in dose units of displacements per atom (dpa). The use of both neutron and ion methods is useful to understand the effects of irradiation dose rate on microstructural evolution processes, including irradiation enhanced precipitation, and to properly interpret results from experiments using accelerated-damage experiments with ions. Here we report on precipitation in Fe-Cu and Fe-Cu-Mn alloys irradiated at dose rates ranging from $\sim 10^{-10}$ dpa/s (neutrons) to $\sim 10^{-5}$ dpa/s (70 MeV Fe ions). Atom probe tomography, small angle neutron scattering, and rate theory models show that precipitation is affected by both dose rate and alloy composition. We report on the experimental results and provide an understanding of the observed trends using rate theory models.

2. EXECUTIVE SUMMARY OF MAJOR RESULTS

1. Preliminary study of carbide precipitation in 316 SS using CD modeling indicates that ballistic mixing could lead to a significantly reduced carbide volume fraction under relevant dose rates for some reactors or previous experimental irradiation studies. However, the results are ambiguous due to strong sensitivity of the ballistic mixing effects to the exact thermodynamic driving force for precipitation. This driving force has uncertainties due to possible fitting errors and temperature dependence that are within the ranges relevant for widely varying ballistic mixing response. The observed low carbide volume fractions may therefore be a ballistic mixing effect or an experimental error, or a combination of both. However, higher irradiation dose rate does lead robustly to a higher fraction of vacancy-interstitial recombination, which leads to less precipitation at the same dose when compared to lower dose rate conditions.
2. We identified that in the CD simulation, at very high fluence, the predicted volume fraction of Cu+MNPs is on dislocations. This is physically plausible since the dislocations are the preferred precipitation sites energetically, however, this simulation result is not consistent with the available experiments. Possible reasons are under investigation.
3. Machine learning using Gaussian Kernel Ridge Regression (GKRR) accurately predicts the change in yield stress for compositions and conditions represented within the IVAR/IVAR+ database and random K-Fold cross-validation (CV) suggests little overfitting. However, prediction of new data from the ATR2 dataset shows that the GKRR method hyperparameter optimization is insufficient for robust predictions. Gaussian Process modeling is explored as a method to avoid these issues with GKRR and shows significant promise, but still has errors that are systematic and too large. Multiple paths to improvement are still available and will be explored. (see Sec. 4.2). [5]
4. Experimental study of the precipitation in Fe-Cu and Fe-Cu-Mn illustrates that 1) decrease in the efficiency of radiation enhanced diffusion, due to increased vacancy-self interstitial recombination; and, 2) increase the rate of ballistic mixing that partly dissolves the precipitate constituents. The key parameter is the rate of ballistic mixing relative to the rate that solutes are reacquired by diffusion. The Mn in the ternary alloy traps vacancies and enhances recombination, leading to very different precipitate evolution kinetics.

3. METHODS

3.1 Cluster Dynamics Simulations

Part of the cluster dynamics simulation model has been discussed in previous milestone [6]. The methods are included in this report for completeness.

3.1.1 Basic Cluster Dynamics model

As described in previous milestones, the CD method [7-10] gives the size distribution of clusters by solving a series of ordinary differential equations as follows:

$$\frac{\partial f(n,t)}{\partial t} = \omega_{n-1,n}^{(+)} f(n-1,t) - \omega_{n,n-1}^{(-)} f(n,t) + \omega_{n+1,n}^{(-)} f(n+1,t) - \omega_{n,n+1}^{(+)} f(n,t), \quad (1)$$

where

$f(n,t)$ = concentration of clusters containing n atoms at time t .

The coefficient $w_{n,n+1}^{(+)}$ s are the rates at which clusters of size n absorb single atoms to grow to size $n+1$, $w_{n,n-1}^{(-)}$ s are the rates at which clusters of size n emit single atoms to shrink to size $n-1$, and $\Delta G(n)$ is the formation energy of clusters with n atoms. More details regarding this method can be found in Ref. [7-10].

For a system containing k precipitating components, the rates of absorption are given by:

$$\omega_{n,n+1}^{(+)} = \left[\sum_{i=1}^j \left(\frac{v_{i\alpha}^2}{\omega_{n_i;n_i+1}^{(+)}} \right) \right]^{-1}, \quad (2)$$

where

$w_{n_i;n_i+1}^{(+)}$ = rate at which clusters of size n gain one atom of species i .

The parameter $v_{i\alpha}$ accounts for the change in the composition of component i as the cluster grows from size n to $n+1$. It is defined by the following expression:

$$v_{i\alpha} = x_{i\alpha} + n \frac{dx_{i\alpha}}{dn}, \quad (3)$$

where

$x_{i\alpha}$ = atomic fraction of component i in clusters of size n .

Here it is assumed that $x_{i\alpha}$ does not change with n , thus $v_{i\alpha}$ equals $x_{i\alpha}$.

For diffusion-limited growth of the clusters, the absorption rate becomes:

$$\omega_{n,n+1}^{(+)} = 4\pi c_{\beta} a_{\alpha} D_{eff}^d n^{1/3}, \quad (4)$$

$$\frac{1}{D_{eff}^d} = \sum_{i=1}^k \frac{v_{i\alpha}^2}{x_{i\beta} D_i}, \quad (5)$$

where

C_{β} = total volume concentration of the particles of the different components in the ambient phase

$x_{i\beta}$ = molar fraction of the different components in the ambient phase.

The emission rate is given by:

$$\omega_{n+1,n}^{(-)} = \omega_{n,n+1}^{(+)} \exp\left(\frac{\Delta G(n+1) - \Delta G(n)}{k_R T}\right), \quad (6)$$

where

$\Delta G(n)$ = formation energy of clusters with n atoms from the matrix, which can be written as:

$$\Delta G(n) = n(g_p - \sum_i x_i \mu_i) + \sigma(n), \quad (7)$$

where

g_p = free energy per atom of the precipitate phase

μ_i = chemical potential of component I in the matrix

$\sigma(n)$ = interfacial energy of a cluster of size n .

With this form, the difference $\Delta G(n+1) - \Delta G(n)$ reduces to:

$$\Delta G(n+1) - \Delta G(n) = g_p - \sum_i x_i \mu_i + [\sigma(n+1) - \sigma(n)], \quad (8)$$

The chemical potentials can be written as:

$$\mu_i = \mu_i^0 + kT[\ln \gamma_i + \ln c_i], \quad (9)$$

Where γ_i is the activity coefficient. When the matrix phase is in equilibrium with the precipitate phase we have the relationship:

$$\begin{aligned} g_p - \sum_i x_{i\alpha} \mu_i &= 0 \\ g_p - \sum_i x_{i\alpha} [\mu_i^0 + kT \ln \gamma_i] &= kT \sum_i x_{i\alpha} \ln \bar{c}_i \end{aligned} \quad (10)$$

In dilute alloys, the γ_i in Eq. (13) will become constant according to Henry's law, thus according to Eq. (11) - (13), we can obtain

$$\Delta G(n+1) - \Delta G(n) = kT \sum_i x_{i\alpha} \ln \frac{\bar{c}_i}{c_i} + [\sigma(n+1) - \sigma(n)], \quad (11)$$

Substituting Eq. (14) into Eq. (9), the emission rate can be written as:

$$\omega_{n+1,n}^{(-)} = \omega_{n,n+1}^{(+)} \frac{\prod_i \bar{c}_i^{x_i}}{\prod_i c_i^{x_i}} \exp \left(\frac{\sigma(n+1) - \sigma(n)}{k_B T} \right), \quad (12)$$

where $\prod_i c_i^{x_i}$ and $\prod_i \bar{c}_i^{x_i}$ are the solute product and solute product at equilibrium, respectively, and they are represented by K_{sp} and \bar{K}_{sp} , respectively.

The distribution function $f(n=1, t)$ at $n=1$ is described as:

$$f(n=1, t) = c_\beta \prod_{i=1}^k x_{i\beta}^{x_{i\alpha}}, \quad (13)$$

3.1.2 Simulation Models for carbide precipitation in Austenitic stainless steels

3.1.2.1 Thermodynamics

The carbides formed in the 316 SS at around 300 °C are $M_{23}C_6$ and M_6C . The composition of the 316 stainless steel used in this study is listed in Table 1. CALPHAD predictions of Carbide composition change as a function of temperature, using OCTANT database [11], are shown in Figure 1. Results show minor changes in composition with temperature. Thus, to simplify the model, we approximately treat the carbides as line compounds with compositions shown in Figure 1. Specifically, at 320 °C, the composition is $Cr_{0.562}Mo_{0.102}Fe_{0.129}C_{0.207}$ for $M_{23}C_6$, and $Cr_{0.047}Mo_{0.543}Fe_{0.274}C_{0.137}$ for M_6C .

The interfacial energies between the carbides and the matrix are not available experimentally. Thus, we take the value predicted by OCTANT using the nearest-neighbor broken bond method [4], $\gamma_{M_{23}C_6-Fe} = 0.25 \text{ J/m}^2$, $\gamma_{M_6C-Fe} = 0.35 \text{ J/m}^2$.

Table 1 Chemical composition of typical 316 stainless steel.

Element	Fe	Cr	Ni	Mn	Si	C	Mo
Composition (wt%)	Bal.	16.6	10.6	1.12	0.68	0.054	2.25

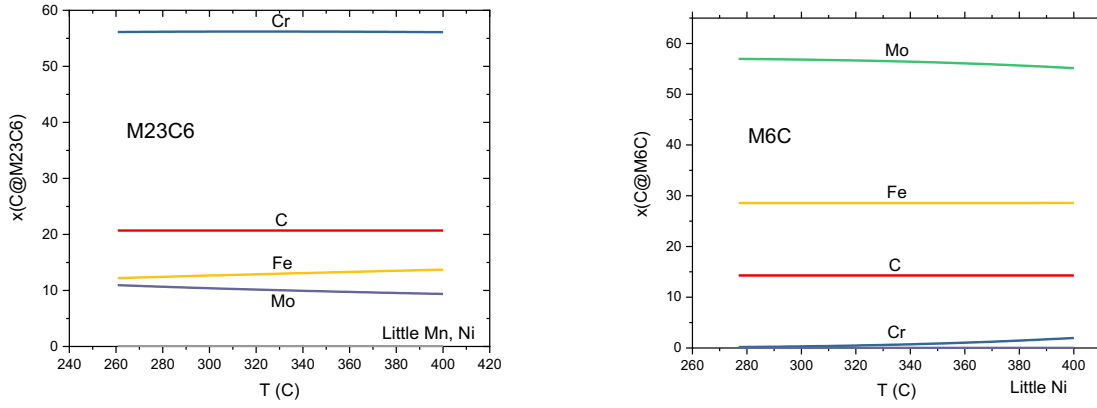


Figure 1. Temperature dependence of the carbide composition. (a) $M_{23}C_6$; (b) M_6C

By treating the carbides as line compounds, the equilibrium solute product can be readily calculated as a function of temperature. The calculated equilibrium solute product values are shown in Figure 2. These calculated equilibrium solute product values are later used in the CD model, describing the thermodynamics of the carbide. Note, since in both carbides the main contents are C, Cr, Fe and Mo, we ignore the Mn and Ni elements when calculating the equilibrium solute product.

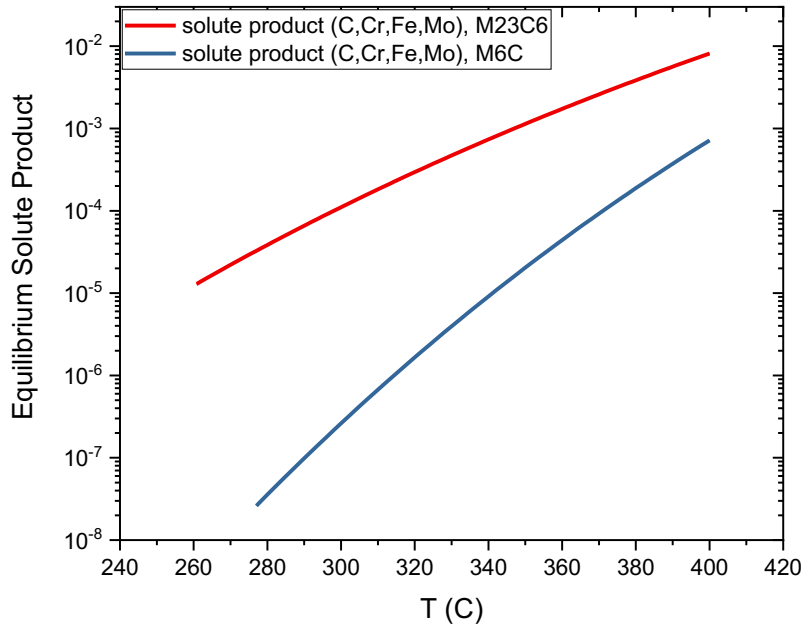


Figure 2. Equilibrium solute product of the carbides.

3.1.2.2 Radiation enhanced diffusion (RED) model

The radiation enhanced diffusion (RED) model used here is based on the one developed by Odette et al. [12]. The radiation enhanced diffusion coefficients are expressed as

$$D^{irr} = D_v X_v \frac{D^{th}}{D^{sd}} + D^{th}, \quad (14)$$

where D^{irr} is the diffusion coefficient under irradiation, D_v is the diffusion coefficient of vacancies, X_v is the vacancy concentration under irradiation, D^{th} is the solute thermal diffusion coefficient of solute under thermal aging condition, and D^{sd} is the self-diffusion coefficient of Fe in the matrix.

Defect conservation balances, treating vacancy and SIA production, transport and fate, were used to establish the steady-state vacancy concentration (X_v) under irradiation, which can be expressed from rate theory models as a function of the fraction of vacancies and self-interstitials (SIA) that escape recombination and reach fixed dislocation sinks (g_s), which is given as:

$$X_v = \frac{g_s \xi \sigma_{dpa} \phi}{D_v S_t}, \quad (15)$$

Here, ϕ is irradiation flux, σ_{dpa} is the displacement-per-atom (dpa) cross-section, ξ is the fraction of vacancies and SIA created per dpa. Assuming that defect recombination occurs as vacancies and SIA diffuse freely through the ferrite matrix it can be shown that

$$g_s = \frac{2}{\eta} [(1 + \eta)^{1/2} - 1], \quad (16)$$

$$\eta = \frac{16\pi r_v \xi \sigma_{dpa} \phi}{\Omega_a D_v S_t^2}, \quad (17)$$

Here, r_v is the SIA-vacancy recombination radius, Ω_a is the atomic volume, and S_t is sink strength.

We will assume that the precipitate growth is dominated by vacancy mediated diffusion of solutes to the precipitates, so correct modeling of the vacancy concentrations and associated RED is critical. Vacancy fates include clustering, annihilation at sinks and recombination with SIA. The dominant fixed sinks for vacancies are typically dislocations. Other sinks include dislocation loops, which are also dose/dose rate dependent. Modeling the detailed evolution of the size/number density of dislocation loops is complex. However, it has been shown that in austenitic stainless steels, the dislocation loop structures often saturate and reach a steady state at higher fluences. Thus, for simplicity, in this preliminary stage of the study, we treat the dislocation loops as a fixed sink. The total sink strength of the dislocation plus the dislocation loops is taken as $2 \times 10^{14} \text{m}^{-2}$ [13].

The thermal diffusion coefficients of carbide components in 316 SS at 320 °C can be found in Ref. [4], and they are listed in Table 2. To obtain η , the constants used in the simulations are $r_v = 0.57$ nm, $\xi = 0.3$, $\sigma_{dpa} = 1.5 \times 10^{-25} m^2$, Ω_a is the atomic volume $1.18 \times 10^{-2} nm^3$, D_v is the vacancy diffusion coefficient, $10^{-4} \times \exp(-1.3/T)$ m²/s and S_t is the dislocation density, taken here as $2 \times 10^{14} m^{-3}$ [4].

Table 2 Thermal diffusion coefficients of carbide components in 316 SS at 320 °C [4].

Element	Tracer diffusion coefficient (m ² /s)
C	6×10^{-20}
Cr	1×10^{-29}
Fe	9×10^{-30}
Mn	8×10^{-29}
Mo	2×10^{-29}
Ni	2×10^{-30}

3.1.2.3 Ballistic mixing

As discussed previously, a precipitate can emit monomers as a result of thermal dissociation. For a system under irradiation, the emission can also result from irradiation induced ballistic mixing. As shown by Xu et al. [14], within the framework of the traditional cluster dynamics model, the ballistic dissolution rate can be superimposed onto the thermal dissociation rate. By introducing a precipitate size-independent cascade re-dissolution parameter (*SICRD*), the ballistic dissolution rate can be written as

$$w_b = SICRD \times \frac{4\pi}{3} (r_n + a_0)^3 \times \phi \times \frac{\partial^2 N_{PKA>1keV}}{\partial l \partial N}. \quad (18)$$

The value of *SICRD* can be determined by molecular dynamics simulations, and is approximately 1 per PKA (Primary Knock-on Atom) [15]. $\frac{\partial^2 N_{PKA>1keV}}{\partial l \partial N}$ is the number of PKAs (>1keV) created per incident particle per unit depth. Adding the ballistic dissolution rate onto the normal thermal dissociation rate, the cluster dynamics model can keep its original form.

The $\frac{\partial^2 N_{PKA>1keV}}{\partial l \partial N}$ term can be determined by SRIM in the ion irradiation case [14]. However, the method does not apply to the neutron irradiation situation. The $\frac{\partial^2 N_{PKA>1keV}}{\partial l \partial N}$ term is essentially a PKA rate (in unit of PKA/cm³·s). For a first approximation, we take the modified Kinchin-Pease model to calculate the number of displacements per PKA, then we use this value to convert a certain damage rate (in unit of dpa/s) to a PKA rate. The modified Kinchin-Pease model can be written as

$$N_d(T_d) = \begin{cases} 0 & , \quad T_d < E_d \\ 1 & , \quad E_d < T_d < 2E_d / 0.8 \\ \frac{0.8T_d}{2E_d} & , \quad 2E_d / 0.8 < T_d < \infty \end{cases} \quad (19)$$

PKA rate can be written as

$$\int_{E_d}^{\infty} \frac{\text{displacement rate}}{N_d(T_d)} \frac{\partial \sigma}{\partial T_d} dT_d \quad (20)$$

where $\frac{\partial \sigma}{\partial T_d}$ is the differential normalized primary knock-on spectra for the particular irradiation. For simplicity, as a coarse approximation, we use T_d as $T_{1/2}$ (median in the PKA spectra), eliminating the integral. Thus

$$\text{PKA rate} = \frac{\text{displacement rate}}{N_d(T_{1/2})}. \quad (21)$$

For steel, $E_d = 40\text{eV}$. Taking $T_{1/2}$ to be 50keV as an example, the PKA rate = displacement rate/500.

3.1.3 Simulation Models for the ferritic low-alloy RPV steels

3.1.3.1 Heterogeneous nucleation

In our previous milestone, we showed that homogeneous nucleation is inadequate to match the experimentally observed MNS precipitates number density in Cu-free alloys and some form of in-cascade MNS precipitation is needed. Similarly, Monte Carlo simulations [16] show Cu will precipitate in cascade in FeCu binary alloys. In addition to in-cascade precipitation, formation of Cu and Cu-MNS precipitates on dislocations have been observed both in experiments [17] and simulations [18]. These results suggest the need for both in-cascade and on dislocation heterogeneous dislocation in addition to homogeneous nucleation. Heterogeneous nucleation at

grain boundaries was not considered in the present study because the number of grain boundary nucleation sites are much smaller than those associated with cascades and dislocations for RPVs and will make a negligible contribution to high-fluence precipitate number densities (see Sec. 3.1.3.1.3).

3.1.3.1.1 Nucleation in cascade

For nucleation in cascade the precipitates nucleation rate is proportional to cascade production per atom $\sigma_{cas}\theta/\Omega$ (irradiation term) and ratio of the instantaneous solute product to reference solute product, $K_{sp}(t)/K_{sp}^0$ (thermodynamics term). For simplicity we assume that cascades produce only one size precipitates. Therefore, the nucleation rate in cascade is

$$R_{het}(n_{het}, t) = \alpha \cdot \sigma_{cas}\theta/\Omega \cdot K_{sp}(t)/K_{sp}^0 \quad (22)$$

And $R_{het}(n \neq n_{het}, t) = 0$

where α is cascade cluster production efficiency factor, σ_{cas} is the cascade production cross section, θ is the neutron flux, and Ω is the atomic volume, $K_{sp}(t)$ is instantaneous solute product and K_{sp}^0 reference solute product.

With the cascade induced nucleation the general equation for cluster dynamics becomes:

$$\begin{aligned} \frac{\partial f(n, t)}{\partial t} = & R_{het}(n, t) + \omega_{n-1, n}^{(+)} f(n-1, t) - \omega_{n, n-1}^{(-)} f(n, t) \\ & + \omega_{n+1, n}^{(-)} f(n+1, t) - \omega_{n, n+1}^{(+)} f(n, t) \end{aligned} \quad (23)$$

3.1.3.1.2 Nucleation on dislocation

It is known that dislocations are favorable nucleation sites for second phase precipitation because precipitate formation on dislocation releases the excess free energy associated with the dislocations [19]. To account the effect of dislocations on nucleation we combine the CD model with the theory of heterogeneous nucleation on dislocations that was originally developed by Cahn [19]. Considering the effect of dislocation nucleation on CD model the Eq. (7) will be,

$$\Delta G(n) = n(g_p - \sum_i x_i \mu_i) + \sigma(n) + \Delta G_{dist}(r_p) \quad (24)$$

where the last term corresponds to the released excess free energy associated with the nucleation of a precipitate on dislocation and can be given as [19],

$$\Delta G_{disl}(r_p) = \begin{cases} \int_{-r_p}^{r_p} [E_{core}] dl, & r_p < r_{core} \\ \int_{-r_p}^{r_p} [E_{core} + \frac{\mu b^2}{4\pi} \ln(\frac{r(l)}{r_{core}})] dl, & r_p > r_{core} \end{cases} \quad (25)$$

where r_{core} and E_{core} are respectively the dislocation core radius and core energy, r_p is the precipitate radius, r is the distance between a point on the precipitate interface and the dislocation line, l is the distance from the center of a precipitate along the dislocation line, and μ is elastic shear modulus.

Considering the typical size of Cu-MNS precipitates in RPVs (~3-4 nm) we approximate that no precipitate would nucleate within a distance of 5 nm from any evolving precipitate to avoid precipitates overlap. This assumption constrains the total available nucleation sites on dislocations by effectively dividing the dislocation line length by 5 nm, which for a typical RPV dislocation densities ($2 \times 10^{14} \text{ m}^{-2}$) yields a nucleation site density of about $4 \times 10^{22} \text{ m}^{-3}$.

3.1.3.1.3 Nucleation on grain boundaries

Heterogeneous nucleation at grain boundaries was not considered in the present study because the concentration of grain boundary nucleation sites are expected to be much smaller than those associated with dislocations for RPVs. Assuming cubic grains, for an average grain size of $L = 50 \text{ }\mu\text{m}$ and an effective grain boundary thickness where heterogeneous nucleation can occur of $\delta = 1 \text{ nm}$, the potential nucleation sites at grain boundaries are $N = C_0 \frac{\delta}{L} \sim 16 \times 10^{23} \text{ m}^{-3}$, where C_0 is the number of atomic lattice sites per unit volume [20]. However, if we assume the distance of $d = 5 \text{ nm}$ between precipitates the available nucleation sites at grain boundaries would be reduced by at least $N \frac{a^2}{d^2} \sim 5.2 \times 10^{21} \text{ m}^{-3}$ where, N is the potential nucleation sites, a is the lattice parameter, and d is the distance between precipitates.

3.1.3.1.1 Further notes on present excluded volume model for nucleation of precipitates

In the course of very recent discussions we have identified a number of minor issues with the nucleation model. As noted in the above discussions, the number of available sites for nucleation on both dislocations and grain boundaries has been modified by a parameter d , representing the smallest allowed distance between precipitates, or equivalently, an exclusion distance between precipitates. We have used d to modify the available nucleation sites in the dislocation and grain

boundary models, where otherwise very large densities might occur. The first issue is that presently the modification is done at time zero and a modified nucleation site density is used in the simulation. However, a more rigorous model would evolve the nucleation site density in response to the precipitate density, as exclusion can only happen after a precipitate has formed. We do not expect this approximation to have a large impact, but the more rigorous model should be implemented in the future. A second issue is that the present model for the grain boundary sites in the presence of exclusion only consider the exclusion for the plane of grain boundary, and a more detailed consideration of the connection between grain boundary thickness and precipitate exclusion should be established. Given the small contribution to average precipitate size, number density, and volume fraction expected from grain boundaries this analysis is unlikely to have any significant impact. As a third and final issue, we note that a more rigorous model would include exclusion in the bulk in a manner consistent with the treatment of dislocations and grain boundaries. Given the typically lower number densities of bulk vs. dislocation and grain boundary precipitate concentrations the present approximation of ignoring exclusion in the bulk is a small approximation but a modification to have a fully consistent model should be developed. These changes will be introduced as part of general improvements planned in the model (see Sec. 6).

3.1.3.2 Radiation enhanced diffusion (RED) model

The RED model is similar to the one described in Sec. 3.1.2.2. However, in the ferritic low-alloy steels, the UMDs also act as vacancy sinks and can be dominant at very high flux. Furthermore, recombination will be greatly enhanced if vacancies are strongly bound to these UMDs. Odette et al.[12] have built a model to include the effect of UMD in the recombination-dominated regime under very high irradiation flux. This irradiation flux effect can be simply described by adjusting g_s by a scaling law as

$$g_s(\phi) \approx g_s(\phi_r) \left(\frac{\phi_r}{\phi} \right)^p, \quad (26)$$

Here, ϕ_r is a reference flux and p is a scaling exponential factor. The effective p starts at 1 in the thermal diffusion dominated regime at very low flux; p is 0 in the sink-dominated regime and $p=0.5$ in the recombination-dominated regime. The p again approaches 1 at high flux in the UMD sink-dominated regime. We will use this scaling law expression in our model to effectively include the effects of UMDs on the vacancy concentrations.

3.1.4 Parameters for the MNSP Cluster Dynamics model

All the parameters used in the cluster dynamics model for MNSPs are given in this section, and most of them are the same as were reported in the previous milestone. The only differences are the reference solute product and heterogeneous nucleation generation rate coefficient in Sect. 3.1.3.1.1. Instead of choosing 0.01 as the reference solute product, 2.4×10^{-3} is chosen, as a result the heterogeneous nucleation generation rate coefficient has been changed to 7.2×10^{-3} from 0.03, so that their ratio stays the same. As can be seen from Eq. (16), the model stays the same as long as the ratio between reference solute product and heterogeneous nucleation generation rate coefficient doesn't change. The purpose of this change was so that the reference solute product is close to the equilibrium solute product around 290°C (in Table 3), which allows us to interpret the heterogeneous nucleation generation rate coefficient as the number of MNS clusters that will be generated per cascaded in the equilibrium state. The equilibrium solute products of the two phases studied at different temperatures are obtained from the TCAL2 database [21]. These equilibrium solute products at different temperatures are listed in Table 3. Note that the equilibrium solute product here for T6 are calculated with composition of 51.1%Ni-33.3%Mn-15.6%Si, since for the alloys studied here the predicted equilibrium compositions of T6 vary over a Ni composition of just 51%-52%.

Table 3 Equilibrium solute product for each phase at different temperatures

Temperature (°C)	Equilibrium solute product ($\times 10^{-3}$)	
	T3	T6
280	1.96	2.33
284	2.12	2.53
290	2.21	2.56
300	2.45	2.82
400	6.26	6.57
425	7.86	7.95

The thermal diffusion coefficients of Mn, Ni, Si and Fe in ferromagnetic Fe used in this paper are summarized in Table 4.

Table 4 Diffusion coefficients under thermal condition.

Element	D_0 (cm ² /s)	Q (kJ/mol)	Reference
Mn	1.49	234.0	[22]
Ni	1.4	245.6	[23]
Si	0.78	231.5	[24]
Fe	27.5	254.0	[25]

All other parameters are listed in Table 5. Most of them are obtained from two papers [12, 26]. Four of them, heterogeneous nucleation size and rate coefficient (see Sec. 3.1.2) and two interfacial energies are fitting parameters. These parameters were fitted to 28 experimental data points of precipitate number density, mean radius and volume fraction for alloys under different irradiation conditions by mapping a fine grid of the values of these parameters in reasonable range, and the optimal set of parameters were obtained for parameter values where the smallest root mean square difference (RMSD) between simulation results and experimental data was realized.

Table 5 Parameters used in calculating radiation enhanced diffusion coefficient and other parameters.

SIA – vacancy recombination radius (r_v , nm)	0.57 [12]
Fraction of vacancies and SIA created per dpa (ξ)	0.4 [12]
Displacement-per-atom (dpa) cross-section (σ_{dpa} , m ²)	1.5×10^{-25} [12]
Atomic volume (Ω_a , m ³)	1.18×10^{-29}
Vacancy diffusion coefficient pre-exponential factor (D_v , m ² s ⁻¹)	1×10^{-4} [26]
¹⁾	
Vacancy migration energy (E_v^m , eV)	1.3 [26]
Dislocation sink strength (dislocation density) (ρ , m ⁻²)	2×10^{14} [12]
Flux effect scaling exponential factor (p)	0.2 [27]
Cascade cross section ($\sigma_{Cascade}$, m ²)	2×10^{-28} [27]
Reference solute product (K_{sp}^0)	2.4×10^{-3}
Heterogeneous nucleation size (n_h) (FITTED)	60
Heterogeneous nucleation generation rate coefficient (α) (FITTED)	7.2×10^{-3}

Interfacial energy of T3 phase (σ_{T3} , J/m ²) (FITTED)	0.190
Interfacial energy of T6 phase (σ_{T6} , J/m ²) (FITTED)	0.175

3.1.5 Parameters for the Cu-MNS Precipitates Cluster Dynamics model

Formation of pure Mn-Ni-Si precipitates (MNSPs) in RPV steels is limited to Cu-free or very low Cu bearing (Cu<0.06 at.%) alloys and was addressed in Ref. [13] and previous milestones. However, there exist some level of Cu in major in-service RPV steels and its concentration can reach up to 0.25at.% [28]. In the presence of Cu, it is seen that MNSPs are usually spatially correlated with Cu-rich precipitates (CRPs) in RPV steels [29-33]. Note that here we define a CRP as a primarily Cu containing precipitate, but one that also includes other solutes (e.g., a Cu core with Mn, Ni and Si atoms coating it). In the method section, we described the general cluster dynamics model for single and multicomponent precipitates formation. In this section, we expand the CD model to treat the precipitation of Cu along with Mn-Ni-Si. The coupling of Cu and MNSPs is necessary to fully understand their combined impact on the embrittlement of RPV steels

CRPs will form in alloys containing more than ~0.06 at.% Cu. The mechanism for formation of CRPs in the presence of MNS is still being explored, but from atom probe observations [34] and our KMC simulations, we propose that the mechanism is as follows. In the early stages of irradiation, Cu clusters precipitate out, then the Mn, Ni, and Si move toward Cu precipitates and coat the Cu precipitates in just a monolayer or so of Mn, Ni, and Si, forming CRPs. The CRPs enrichment in these solutes can be understood and modeled within the framework of both classical thermodynamics [35] and atomistic simulations [16]. As the irradiation continues the Cu depletes in the matrix (due to its very low solubility limit) while Mn-Ni-Si are still supersaturated. During the Cu precipitation and after, Mn, Ni, and Si continue to precipitate out on the CRP, forming an appendage morphology of a well-developed MNSP.

The above process of coupling Cu and Mn-Ni-Si precipitation is highly complex, and all the features could not be readily incorporated into a practical model. Instead, we took an approximate approach that built separate Cu and MNS precipitate models, and then coupled them in a simple manner that mimicked the essence of the above processes, while simultaneously requiring relatively few adjustable parameters (as illustrated schematically in Figure 3). The right branch of Figure 3 shows the MNSP model, uses the theoretical approach from Ref. [13]. The left branch of Figure 3 shows the Cu precipitation model. Finally, the coupling of Cu and MNS precipitation is

shown schematically by the middle branch of Figure 3. The coupling of Cu and MNS is described in some detail here as well as Sec. 4.1.4.

We coupled the Cu and MNSP by assuming that during the Cu nucleation stage any Cu precipitate which has 20 atoms (\sim Cu precipitate critical size) or more has an accompanying MNSP that has a size proportional to the Cu precipitate. This effectively co-nucleates a MNSP with the Cu precipitate. The MNSP is a distinct precipitate from the Cu precipitate in the model, but does not grow independently during this co-nucleation phase as it is pinned to the Cu precipitate size. The ratio of MNSP to Cu precipitate size during this co-nucleation stage is a fitting parameter. When the Cu nucleation stops, we decouple the co-nucleation and let the Cu and MNSP grow separately. The Cu growth after this stage is limited due to the significant Cu depletion in the matrix, but MNSPs continue to grow, which represents the appendage growth. This way of coupling Cu to MNSP is a quite severe approximation and leaves out many features of our understanding of the true mechanism of precipitation described above. Perhaps the most dramatic feature of the approximation is that we replace the complex process of Mn, Ni, and Si segregating to the Cu/Fe interface and then growing as an appendage with a single nucleation event of an MNSP separate from the Cu precipitate. This approximation still captures the key role of Cu catalyzing the nucleation and growth of MNSPs but greatly simplifies the process in ways that may impact the fidelity of the predicted MNSP evolution. The atom probe experiments and KMC simulations show that Cu precipitates are coated with Mn, Ni, and Si atoms, which means the Cu precipitate is really a CRP, and CRPs will have a different interfacial energy than pure Cu precipitates and pure MNSP. Therefore, we considered the interfacial energy of CRPs (Cu clusters bigger than 20) to be the average of a Cu and MNSP interfacial energy. We note that we tested the sensitivity of the results to this parameter and found very little variation in results by shifting this number between Cu interfacial energy to MNSP interfacial energy. At this stage we assess the impact of the model approximations by determining to what extent we can model a large body of Cu+MNSP evolution data, and the relatively good success we have compared to the experimental data (see Sec. 4.1.4) supports that our approach has captured the essential elements of the Cu+MNSP coupling.

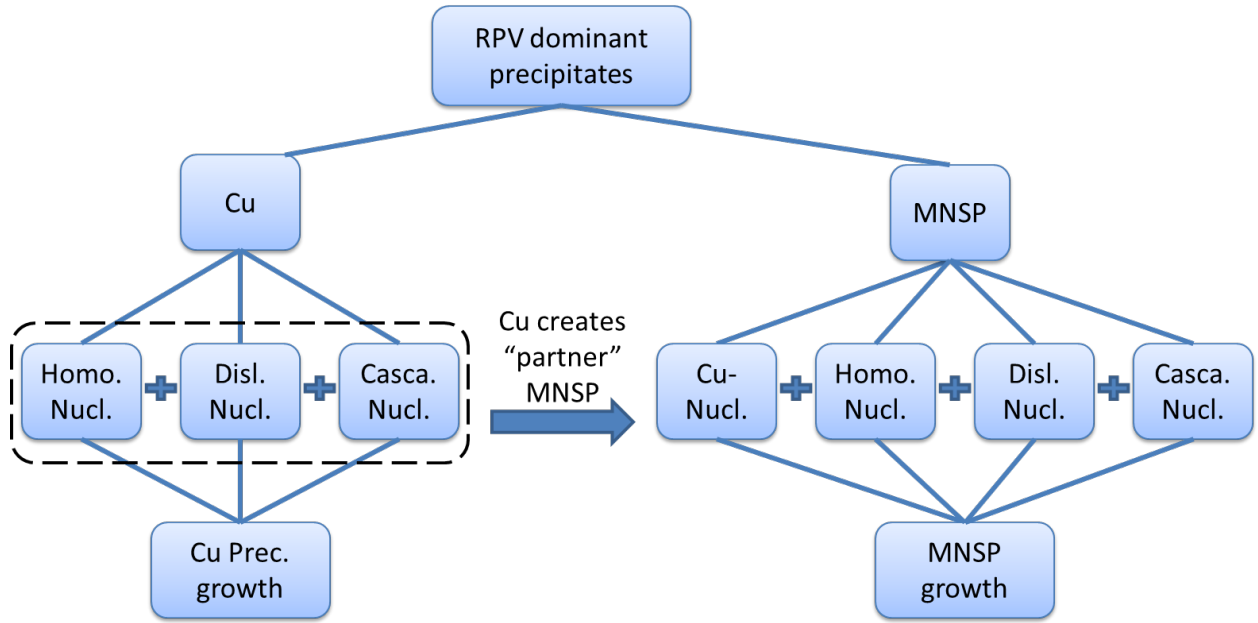


Figure 3. A flowchart of precipitate formation in RPVs in the presence of Cu.

3.2 Machine Learning

3.2.1 Introduction

In addition to the physics-based methods pursued above, we have also used machine learning and data mining to produce a generalizable model for predicting the effect of irradiation on RPV hardening. Previously, Castin et al. used artificial neural network (ANN) techniques to model hardening based on the RADAMO database (SCK•CEN), with a mean predictive error of 45 MPa; however, they note that there is room for improvement of the extrapolative ability of the model, particularly as the principal composition variables ended up being only Cu and Ni content, and the elemental compositions in the database did not vary independently.[36] Kemp et al. similarly used ANN to model and predict yield stresses based on published irradiated steel data taken over a wide-range of temperatures, and had quite large errors in their model. The authors noted that the high errors for some dose rate and temperature ranges could be improved with additional data; that particular strengths of the model were its generalizability over alloys and its ability to give uncertainty estimates, which could then inform selection of additional data points for experiment; and that additional modeling approaches which could incorporate known physics could be complementary.[37] Our analysis is distinct from previous work in that it is using a very extensive dataset that is more focused on data relevant for RPV steels, including a more restricted

composition range and temperature range than some of the above studies, and we are using a somewhat different set of approaches.

To complement the previous ANN studies, the present work uses primarily a more constrained Gaussian Kernel Ridge Regression (GKRR) model, requiring optimization of only two hyperparameters, along with physically based and empirically based descriptors taken from literature [12, 38]. We also consider a related Gaussian Kernel Gaussian Process (GP) model. This model functions in some ways similarly to the GKRR model but offers a few key improvements in usability. The model frameworks can be reapplied to produce different model forms as more data and descriptors become available. Additional data would take the form of more test data points at other compositions, flux, or fluence. Additional descriptors may be identified and added due to improved high fluence and flux understanding, e.g., effective fluence [12]based descriptors.

3.2.2 Model introduction

We develop a generalizable machine-learning model using the information available from the IVAR database, namely the elemental compositions of Cu, Ni, Mn, Si, P, and C, irradiation temperature, flux, and fluence, with hardening in MPa as the response. Flux and fluence are combined into an effective fluence defined by a p -value,[12]

Gaussian Kernel Ridge Regression (GKRR) was implemented through the Python[39] package scikit-learn,[40] and produces a model from these descriptors. The radial basis function (RBF, or Gaussian) kernel determines the distance between feature vectors, and is characterized by hyperparameter γ , where the value of the kernel $K(x, y) = \exp(-\gamma\|x - y\|^2)$, where small values of γ increase the tolerance of what feature vectors are considered similar, and the weighting induced by the kernel is smoothed out over a larger area of feature space. Ridge regression performs linear regression in the kernel and data space (which will be a non-linear function in original space when using a non-linear kernel) and uses the hyperparameter α as the coefficient of an L2 norm penalty in the ridge regression. The hyperparameter α can decrease the sensitivity of the fit to random error in cases where the descriptors have some interdependence, with larger α allowing less sensitivity and penalizing large coefficients.

The Gaussian Process model (GP) was also implemented through the Python[39] package scikit-learn [40], and employs the same kernel as the GKRR model but instead of using ridge regression uses the kernel to define the covariance of a prior distribution over the target functions and uses the training data to define a likelihood function that is used in it's predictions. The GP model uses

the same γ hyperparameter. The kernel also has a scaling prefactor that can be modified to change the total range of values output from the RBF kernel. This prefactor is set to 1 for the current model because the values predicted have been normalized to have a unit standard deviation, suggesting a unit prefactor is appropriate. In addition to hyperparameters associated with the kernel there is also a noise parameter which can either be specified or optimized by the model. In the current results the noise is set to a very small value that plays a role only to introduce numerical stability.

From experimental IVAR and IVAR+ data provided, we make the following changes before applying the machine learning models:

- Removal of alloy LO, which has identical composition and data as alloy LC but was annealed for different times than other alloys in the database.
- Removed duplicate entries (i.e., entries for the same alloy, flux, fluence, and temperature), with the lower hardening response removed, leaving the larger hardening response. The lower hardening response is typically for an alloy that has been annealed for different times than other alloys in the database.
- Updated the irradiation temperature for alloys CM6, LC, LD, LG, LH, and LI at a flux of 2.3×10^{14} n/cm²/sec and a fluence of 1.1×10^{21} n/cm² from 290°C to 320°C after communication from UCSB (this change is due to the change in temperature recently reported for all the so-called ATR1 irradiations).

In addition to the IVAR and IVAR+ datasets which are used for training models there is an ATR2 dataset which can be used for model validation. This dataset is never included in training and consists of 41 alloys irradiated at a fluence of 1.39×10^{20} n/cm² and a flux of 3.64×10^{12} n/cm²/s. 24 of the alloys are exact composition matches from the IVAR and IVAR+ datasets, and 17 alloys are not exact matches, but whose compositions fall within a bounding box made up by the max and min of each element the IVAR and IVAR+ datasets.

3.2.3 Model fitting method – cross validation

Cross-validation (CV)[41] assesses the predictive ability of the model and its independence from a particular training set by breaking data into training and testing data, fitting only to training data, and then assessing errors on testing data.

For n -fold CV (also known as k -fold CV), the dataset is split into n nominally equal parts, called folds. In a single test, the model is trained on the training data in $n-1$ of the n folds. The model is then used to predict the left-out testing fold, with each fold being left out once. Larger numbers of folds indicate that more data is being used to train the model. The root-mean-squared error (RMSE) for each n -fold CV test is given as the average RMSE over all n of the fold predictions and is referred to here as the “fold-average RMSE”. The test may be repeated several times, with the overall cross-validation RMSE given as the average of the fold-average RMSEs of all the tests. If the number of folds n equals the number of data points N , then the N -fold test does not need to be repeated, since there is no randomization when assigning fold members; this test is equivalent to leave-one-out CV.

3.2.4 Model details

As described above, the available data for regression consists of the elemental compositions of Cu, Ni, Mn, Si, P, and C, irradiation temperature, flux, and fluence, with hardening in MPa as the response. From this data, the descriptors used for regression are as follows, although the regression method described below could be reapplied to different or extended sets of descriptors.

- Atomic percent values of Cu, Ni, Mn, Si, P, and C as reported by the alloy compositions in weight percent. Fe is assumed to be the remainder of the weight balance after the six elements described above.
- Irradiation temperature
- Effective fluence, as calculated from the method in Odette et al.,[12] Because the range of effective fluence spans several orders of magnitude, this descriptor is considered on a logarithmic scale.

Each descriptor is normalized linearly over the total set of training and testing data, using the formula $(x - min)/(max - min)$.

The hyperparameters associated with our approach, using the GKRR model α (alpha) and γ (gamma) parameters, are optimized using a grid search. For the GP model a grid search is used to search for an optimal γ (gamma) parameter. 5-Fold cross validation is done from a range of values and the Root Mean Squared Error (RMSE) is used as the criteria for picking the best value. The other hyperparameters are fixed to reasonable values based on the data being predicted.

3.3 Experimental

3.3.1 Materials and irradiation conditions

The nominal composition of the two alloys used in this study are Fe-0.80at.% Cu and Fe-0.78at.% Cu-1.05at.% Mn. The alloys were solution treated for 17 hours at 775 °C, quenched in a salt bath at 450 °C for 3 minutes, and air-cooled to room temperature. The 290°C ion irradiations were carried out at the Center for Accelerator Mass Spectrometry (CAMS) in Lawrence Livermore National Laboratory. The alloys were irradiated by 70-MeV Fe ions at two different dose rates. The dose/dose rate-depth map was calculated using SRIM (Stopping Range of Ions in Matter) [42] using the Kinchin and Pease option with $E_d = 40$ eV, as shown in Figure 4. APT analysis was carried out at three dpa levels (0.3, 1.1 and 3 dpa) in the higher dose rate condition, and at one dpa level (0.03 dpa) in the lower dose rate condition. These dpa levels correspond to sampling depths in the two samples (0.3, 3.25, 5.0, and 5.9 μm), also shown in Figure 4. The neutron irradiations were at two fluxes of $\sim 8 \times 10^{10} \text{ n}\cdot\text{cm}^{-2}\text{s}^{-1}$ and $\sim 7.5 \times 10^{12} \text{ n}\cdot\text{cm}^{-2}\text{s}^{-1}$, spanning a neutron fluence range from $\sim 5 \times 10^{20}$ to $\sim 10^{23} \text{ n}\cdot\text{m}^{-2}$. The neutron fluence was converted to the dpa unit to compare to the ion irradiation doses. The neutron irradiation flux, fluence and corresponding dose/dose rate conditions are summarized in Table 6. Details about the neutron irradiation experiments are reported elsewhere [43]. Based on previous experience with neutron dosimetry, and considering the dpa dose and location precision in the ion irradiation lift-outs (see below), we estimate that the dose uncertainties are $\sim 20\%$ for the test reactor irradiations and $\sim 30\%$ for the ion irradiations. While these are significant in an absolute sense, we do not believe they have major effect on the conclusions reached in this study.

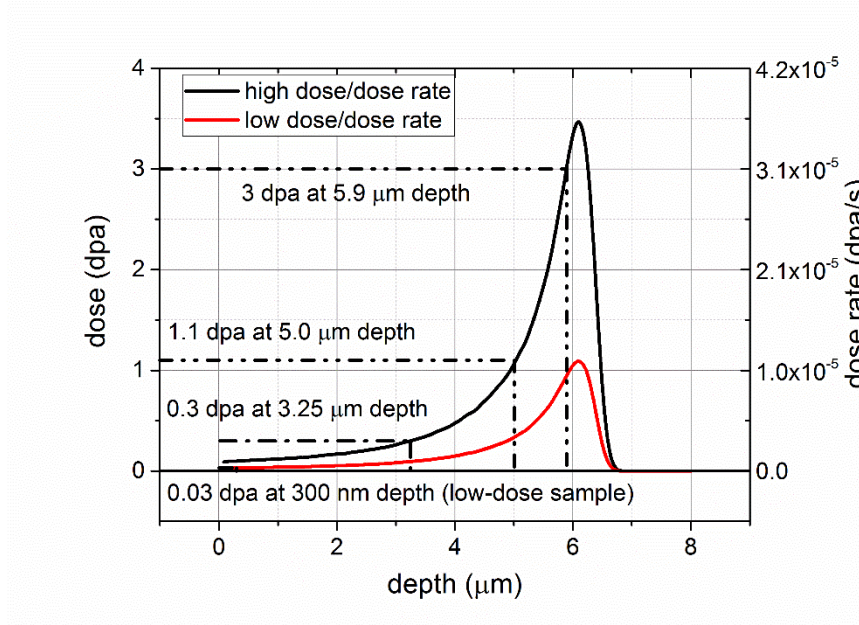


Figure 4 The ion irradiation dose and dose rate as a function of depth below the sample surface, for both Fe-Cu and Fe-Cu-Mn samples. The low-dose sample was used for the 0.03 dpa APT tips; the high-dose sample was used for the 0.3 dpa, 1.1 dpa and 3.0 dpa APT tips.

Table 6 Summary of fluxes and fluences of neutron irradiation.

Name	Flux ϕ ($\text{n}\cdot\text{cm}^{-2}\text{s}^{-1}$)	Fluence ϕt ($\text{n}\cdot\text{cm}^{-2}$)	Dose rate (dpa/s)	Dose (dpa)
L1	8×10^{10}	5×10^{16}	1.2×10^{-10}	7.5×10^{-5}
L2	8×10^{10}	1×10^{17}	1.2×10^{-10}	1.5×10^{-4}
L3	8×10^{10}	2×10^{17}	1.2×10^{-10}	3.0×10^{-4}
L5	8×10^{10}	3×10^{17}	1.2×10^{-10}	4.5×10^{-4}
H1	7.5×10^{12}	4×10^{17}	1.1×10^{-8}	6.0×10^{-4}
H5	7.5×10^{12}	5.1×10^{18}	1.1×10^{-8}	7.7×10^{-3}
H6	7.5×10^{12}	1×10^{19}	1.1×10^{-8}	1.5×10^{-2}

3.3.2 Atom probe tomography

Atom probe tomography (APT) characterization was carried out at University of Wisconsin–Madison on a CAMECA Local Electrode Atom Probe (LEAP) 3000 Si (~57% total detection

efficiency). APT tips were fabricated using a dual-beam focused ion beam (FIB) system (Zeiss Auriga) with standard lift-out method as described in Ref. [44]. After general shaping of the needle at 30 kV, low-energy milling at 5 kV was used to precisely locating tip at the desired depth, which was followed by a final 2 kV clean-up milling to reduce the Ga damage and contamination.

The tips were analyzed using voltage mode at 50 K to mitigate the preferential field evaporation of Cu atoms. The tips were electrically pulsed with a pulse fraction of 20%, a pulse rate of 200 kHz, and a target evaporation rate between 0.5% and 1.5%. A minimum of two tips were studied for each condition. For samples with lower precipitate number density, more tips were analyzed. Reconstruction of the tips were performed using the CAMECA IVAS software (version 3.6.14). The reconstruction used the SEM micrographs to estimate the tip radii along the z-axis. Due to the sample alignment process during initial stage of the evaporation, the data from the very top part of the tip were excluded from the reconstruction. The initial tip radius for the reconstruction was determined by enforcing the measured interspacing distance of (200) and/or (110) planes to be equal to the theoretical value for bcc Fe. Standard value for the image compression factor (ICF = 1.65) and the evaporation field of pure Fe ($E = 33 \text{ V nm}^{-1}$) [45] were used.

To determine the size and composition of the precipitates, cluster analysis was performed using a modified maximum separation algorithm [46], which is based on the fact that solute atoms that belong to one cluster are closer than those within the matrix. The *order* of the method was chosen to be 5, i.e., a solute atom can only be considered as a core atom of a cluster if there are at least 5 solute atoms to be in its proximity (defined by d_{max} , typically $\sim 0.7 \text{ nm}$). More details on determining the order of the method can be found in Ref. [43]. After a core atom is identified, solute atoms within d_{max} of a core atom are included in the cluster. In the last step, matrix atoms around the outside of the cluster are removed using the erosion method [47], with erosion distance

$\sim d_{\max}$. Also, clusters containing less than N_{\min} (typically ~ 30) atoms are ignored, since they are assumed to be a result of random fluctuation in the material [48].

The precipitate sizes (r_p) were calculated by counting the solute atoms in the precipitates, corrected by the detection efficiency, assuming that the solute atomic volume is the same as Fe. The number density (N) of the precipitate was calculated by dividing the number of precipitates by the total reconstruction volume. Precipitates on the edge of the reconstruction volume was not used to calculate the precipitate size, but counted as 0.5 when calculating the number density. Precipitate volume fraction was calculated by dividing the number of solute atoms inside the precipitates by the total number of atoms in the APT reconstruction volume. The average precipitate size, number density and volume fraction were calculated by performing total atom count weighted averaging of measurements from multiple tips. More details on calculating the averages can be found in Refs. [34] and [43].

Note that the atom probe tomography technique has multiple artifacts that can affect the interpretation of the reconstruction results. As shown in many previous studies, trajectory aberration artifacts that spray adjoining matrix atoms into the Cu core lead to artificially high Fe composition in Cu precipitates [49, 50]. Trajectory aberrations result from preferential evaporation of Cu (and other low field emission solutes) that locally flatten or dimple the otherwise hemispherical APT, leading to an unphysically high atomic densities in the precipitates. Trajectory aberration artifacts were recently analyzed for the Fe-Cu/Fe-Cu-Mn alloys by inter-comparing the results of various characterization methods, showing that the precipitates do not contain a significant amount of Fe ($< 6\%$) [43]. Therefore, in this study, only solute atoms are counted when determining the precipitate size and volume fraction.

4. RESULTS

4.1 Cluster Dynamics

4.1.1 Precipitation of Carbides in 316 stainless steels: without irradiation

In this section, we show the CD simulation results on the precipitation process of the carbides in 316 stainless steels under thermal annealing. As shown in Figure 5, at 385 °C the MatCalc simulations (solid line) [4] using OCTANT database predict a relatively rapid formation of a 1.2% volume fraction $M_{23}C_6$, which then gets replaced gradually by M_6C while increasing to a final volume fraction of 1.7% [4]. Note for the modeling results, radiation enhanced diffusion is considered, but that there is no enhancement under thermal annealing. To test the consistency of the CD model with thermodynamic predictions from OCTANT, we simulate with CD the annealing of the 316 steels at 320 °C, starting from a solid solution state. Significant precipitation of carbides is observed. Figure 6 shows the volume fraction, average precipitate radius and the number density of the precipitate as a function of annealing time. We see the same transition sequence in the CD prediction as seen with Octant modeling. In addition, the saturated M_6C volume fraction is also consistent with the OCTANT prediction. Note, the plots of the precipitate radius and number density generally show a nucleation, growth, and dissolution sequence for the $M_{23}C_6$ phase, where the latter corresponds to the shift to a dominant M_6C phase. Also, it is worth noting that at this low annealing temperature, the time needed for significant precipitation is extremely long. Thus, the precipitation of bulk carbides in this alloy observed in the experiments is very likely a direct result of the irradiation enhanced diffusion of the solutes. We also note that in experiments, there have been works looking at both the grain boundary and the grain interior [1-4]. The experimental observations are similar in both cases in that with irradiation, the volume fractions are lower than the thermodynamics predictions. Note that grain boundary precipitation is likely much faster but here we focus on modeling bulk precipitates since the nucleation process is simpler to model.

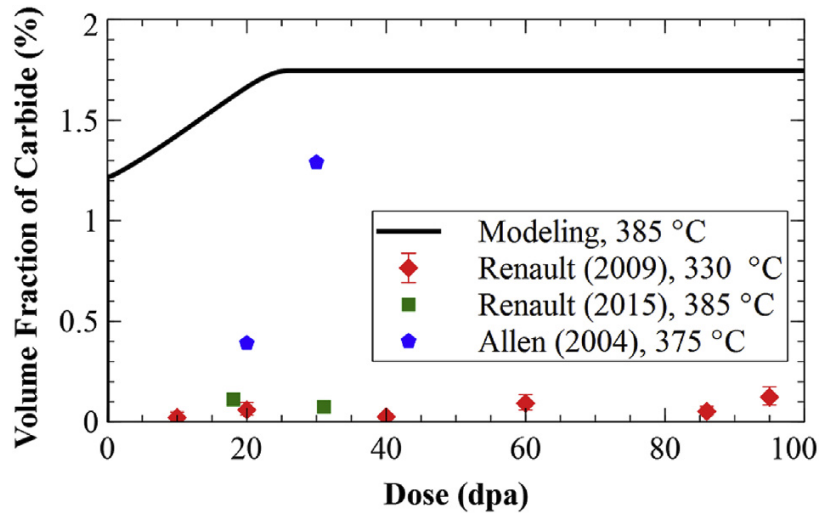
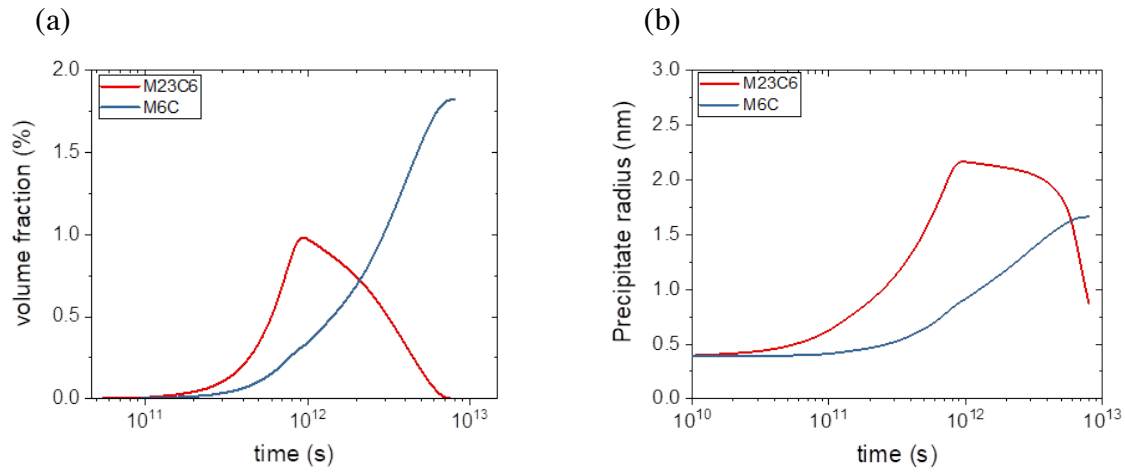


Figure 5 Evolution of total carbides ($M_{23}C_6$ and M_6C) volume fraction compared to experimental data. We note that the nature of precipitates in Renault (2009) were uncertain and could be carbide or G-phase. Adapted from Ref. [4].



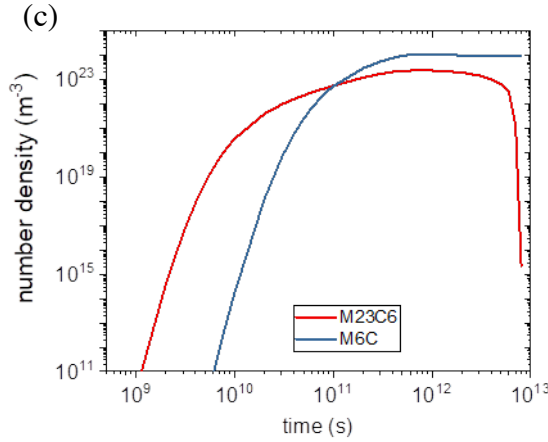


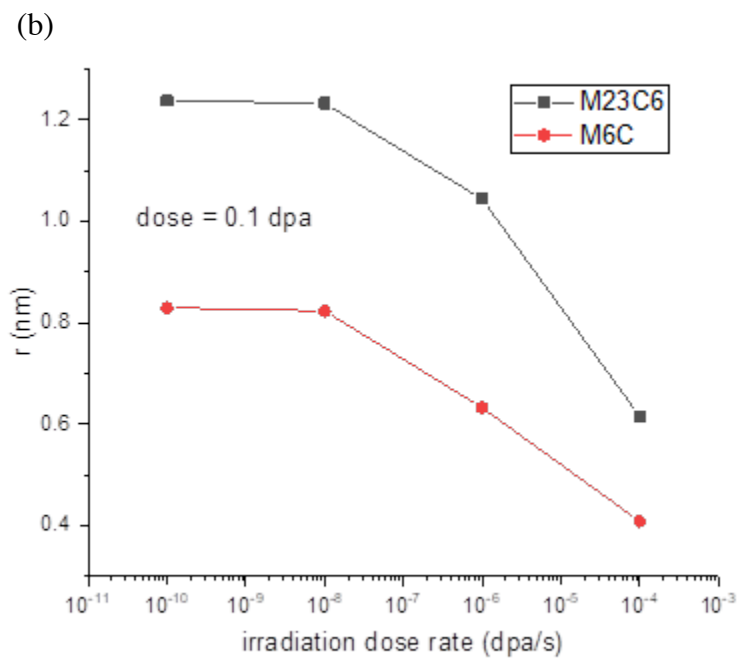
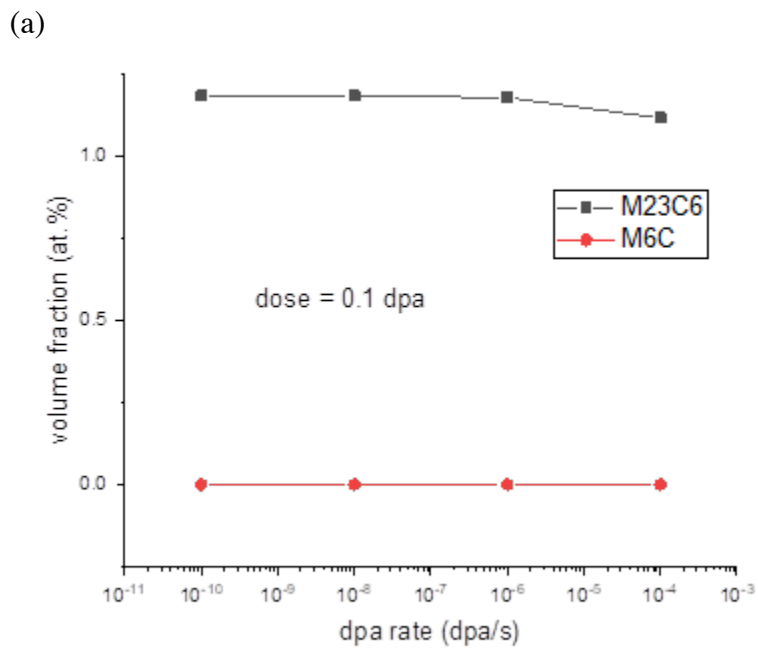
Figure 6. CD simulation of annealing of a 316 SS at 320 °C (a) volume fraction (b) precipitate radius (c) precipitate number density.

4.1.2 Precipitation of Carbides in 316 stainless steels: effect of irradiation

In this section, we show the CD simulation results of the precipitation process of the carbides in 316 stainless steels under irradiation. As stated in Section 1, one of the interesting points from available experiments is that, under irradiation, the volume fraction of the carbides characterized by TEM is often smaller than that predicted by the thermodynamics. For example, Figure 5 shows the comparison of three experiments compared to the thermokinetics prediction. One of the possible reasons of this discrepancy is the ballistic mixing effect, which is directly related to the irradiation dose rate. Higher irradiation dose rate has been shown to be associated with stronger ballistic mixing [51]. The goal of the work during this milestone period has been to assess if ballistic mixing and associated dose rate effects might be impacting the carbide volume fraction.

To assess the dose rate effect, we plot the precipitate volume fraction, radius and number density as a function of irradiation dose rate. Dose rates from 10^{-10} dpa/s to 10^{-4} dpa/s were used. For all cases, significant precipitation of the carbides has been observed. As shown in Figure 7a, at 0.1 dpa, the $M_{23}C_6$ volume fraction is nearly saturated at 1.2% for all dose rates except for the 10^{-4} dpa/s case. However, the transition from $M_{23}C_6$ to M_6C which was observed in the annealing case did not happen at the dose of 0.1 dpa for the irradiated condition. Instead, the M_6C volume fraction is always nearly zero. As suggested by Figure 6, the intrinsic kinetics of the precipitation is very slow. It is thus possible that our simulations to less than 1 dpa are not long enough to reproduce the transition to the more stable carbide, which would be expected at high enough dose.

As shown in Figure 7b, the CD model predicts a smaller radius associating with higher dose rates, which is consistent with the increasing number density trend shown in Figure 7c.



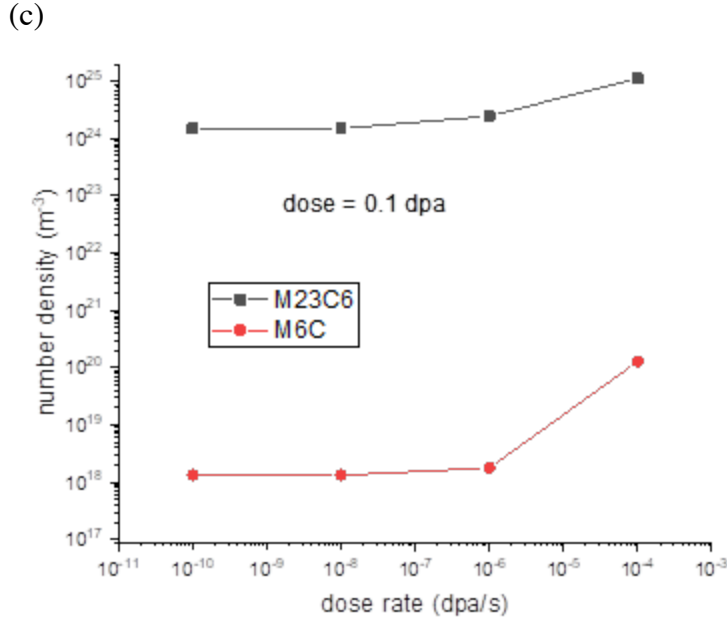
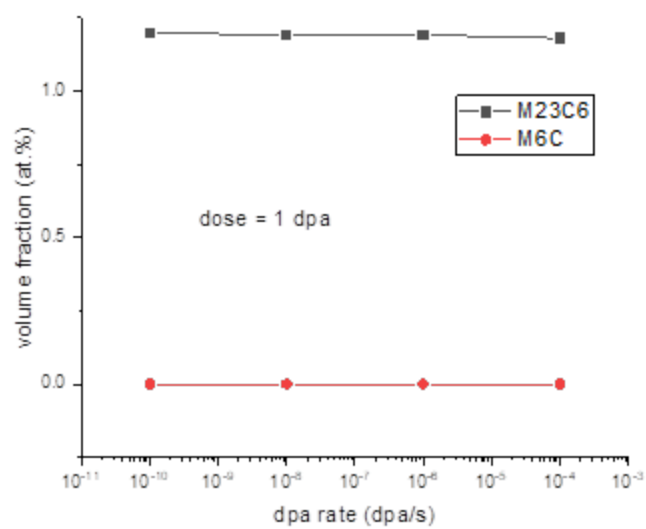


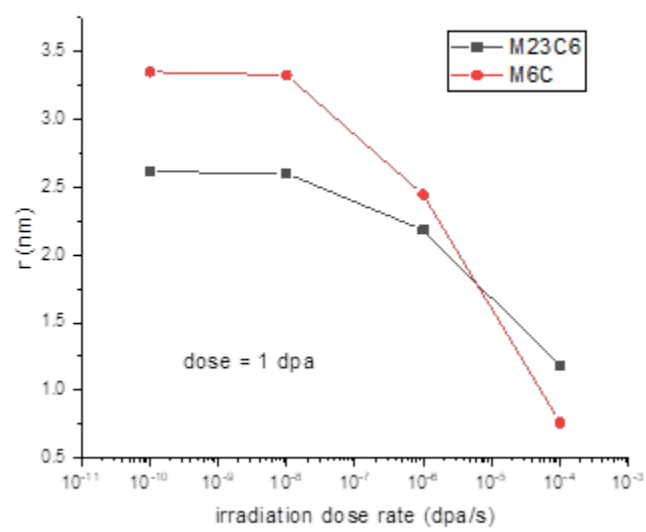
Figure 7. Precipitate evolution at 0.1 dpa (a) volume fraction (b) precipitate radius (c) precipitate number density.

At a higher dose of 1 dpa, as shown in Figure 8a, the M_{23}C_6 volume fraction is fully saturated at 1.2% for all dose rates. Similar to the 0.1 dpa condition, no transition from M_{23}C_6 to M_6C was observed. Again, such a transition is expected at high enough dose. The precipitate sizes are larger, and the number densities are lower, compared to the 0.1 dpa condition at the same dose rate. However, the general trend of the precipitate size/number density evolution is similar to the 0.1 dpa condition. With the volume fraction saturating, the size/number density evolution trend suggests that with higher dose rate, the coarsening does not increase as much with increasing dose as with the lower dose rate. This is likely due to the higher vacancy-interstitial recombination fraction, which yields effectively less diffusion for a given total dose.

(a)



(b)



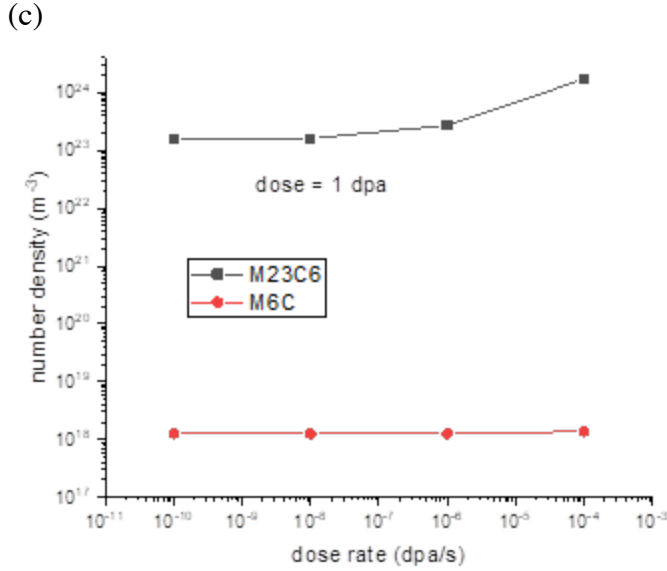
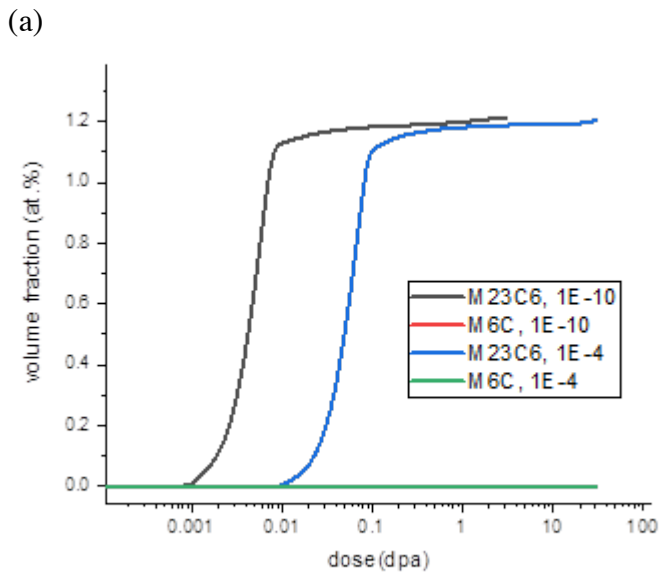


Figure 8. Precipitate evolution at 1 dpa (a) volume fraction (b) precipitate radius (c) precipitate number density.

In Figure 9, the precipitate evolution is plotted as a function of irradiation dose, at two dose rates, 10^{-10} and 10^{-4} dpa/s. For both dose rates, we see the sequence of nucleation, growth and coarsening. Again, it is evident that the precipitation process occurs at lower fluence for the lower dose rate situation and that even the highest flux does not significantly alter the volume fraction at greater than ~ 0.1 dpa in this model.



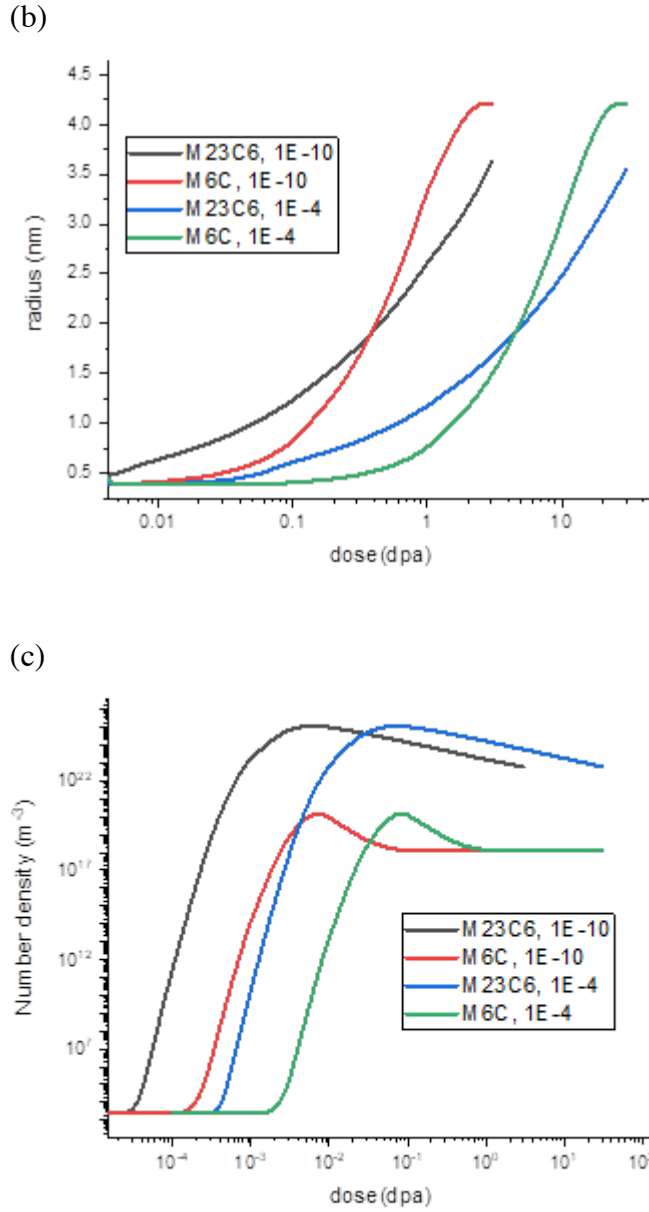


Figure 9. Precipitate evolution as a function of irradiation dose.

These CD model with our specific parameterization and simulated conditions suggests that for a wide range of dose rate values the primary dose rate effect is on radiation enhanced diffusion, and the ballistic mixing does not have a significant effect on the final volume fraction of the carbide phases. This result suggests that the observed reduced volume fraction of carbides compared to that expected from thermodynamic considerations maybe be an experimental artifact, associated with somehow missing significant carbide volume fraction in the characterization. However, the model has significant uncertainties

which turn out to have and significant impact on the conclusions, and we explore those in more detail in Sec. 4.1.3.

4.1.3 Precipitation of Carbides in 316 stainless steels: effect of change of solute product

The thermodynamics of the precipitation process is largely determined by the solute product parameter, which sets the solubility limit of the metal and C relative to the carbide precipitates. It is important to assess the sensitivity of our observations as a function of the solute product as this quantity may have some errors. It has been shown that the solute product is related to the relative free energy of the precipitate phase to the dissolved solutes, which can be written as $\nabla G = kT \ln(K_{sp})$ [13]. Thus, a change in free energy as a function of a change in equilibrium solute product can be written as $\Delta \Delta G = kT \ln\left(\frac{\overline{K'_{sp}}}{\overline{K_{sp}}}\right)$, where $\overline{K'_{sp}}$ is the changed equilibrium solute product. Based on this, a 2, 3, 4 and 5-fold increase of the equilibrium solute product leads to a change of free energy of $\approx 40, 60, 70$, and 80 meV/atom of $M_{23}C_6$ at 320°C (Note that the precipitate formation energy $\Delta G = kT \ln(K_{sp})$ is approximately 400 meV). We focus on 320°C as that is the temperature for which our model fitting was carried out and it is therefore where we expect the most physically robust model. We consider a flux of 10^{-6} dpa/s, which is close to that used in relevant experimental studies (9.4×10^{-7} dpa/s)[52], which studies were also done at 330°C , similar to the temperature we are modeling. CD tests show that a 3-fold increase of equilibrium solute product is unable to destabilize the precipitate under irradiation of 10^{-6} dpa/s at 1 dpa and shows almost no effect on volume fraction, see Figure 10. However, under the same condition, with a 4-fold increase of equilibrium solute product, no stable precipitate appear to form at any dose up to 10 dpa.

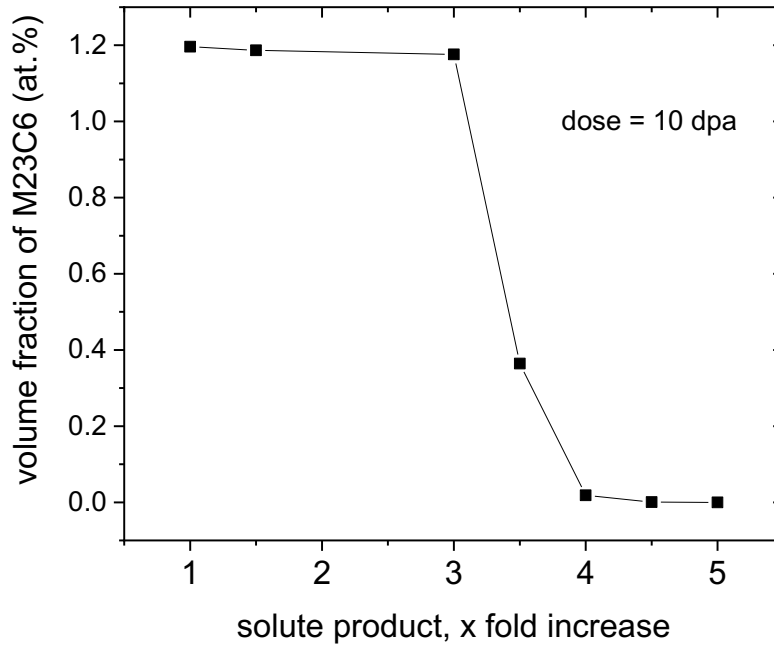


Figure 10. volume fraction of $M_{23}C_6$ at 10 dpa, plotted as a function of solute product increase.

This strong dependence of volume fraction on solute product was unexpected and has significant implications for the result. First, it suggests that temperature effects of just ~ 20 degrees could play a significant role on the stability of the carbides under varying flux, since the $M_{23}C_6$ (M_6C) solute product can vary by $3\times$ ($6\times$) over this temperature range (see Figure 2). Second, it suggests that relatively minor errors in low temperature solute products may have a significant influence on the results. Given this role of temperature and sensitivity, a more detailed study that attempts to exactly match temperature and flux conditions of the experiments and provide validated solute product values would be valuable. We have not pursued such efforts within the scope of the present modeling given its approximate nature and dependence on fits developed at 320°C , but such an extension of the present work is of interest for future study.

4.1.4 Precipitation of Cu-MNS in RPV steels

In Figure 11 we compare the CD model results and the experimental data used in fitting the model for evolution of precipitates in LC, LD, LH, and LI alloys as a function of fluence. In these plots, we run the CD code for an average environment condition (1×10^{16} n/m²/s, 290°C) to get a smooth average trend (yellow line) and run the CD code for all specific experimental data

conditions to give the best possible comparison (green triangle points). The experimental data given in Figure 11 are obtained via small angle neutron scattering (SANS) measurements. To consistently compare the CD results with SANS data we follow the SANS data post processing for CD data, which is fitting the particle size distribution (PSD) to a log-normal distribution and then using the log-normal distribution function to extract the particles number density and mean size. To get the log-normal distribution function we fit the μ and β (mean and standard deviation of the variable's natural logarithm, respectively) of log-normal distribution somehow its first and second moments match with the first and second moment of the CD particle size distribution. After fitting the CD PSD with a log-normal distribution, we calculate particles mean size and number density as following.

$$\langle r \rangle = \left[\frac{\int n(r)r^3 dr}{\int n(r)dr} \right]^{1/3} \quad (27)$$

$$N = \int n(r)dr \quad (28)$$

where $n(r)$ is the log-normal fit function of CD particle size distribution.

$$n(r) = \frac{N^*}{r\beta\sqrt{2\pi}} e^{-\frac{(\ln(r)-\mu)^2}{2\beta^2}} \quad (29)$$

N^* in above equation is calculated somehow the Eq. 25 gives equal particles number density for CD and log-normal fit function for particle sizes in SANS resolution range (size > 1 nm).

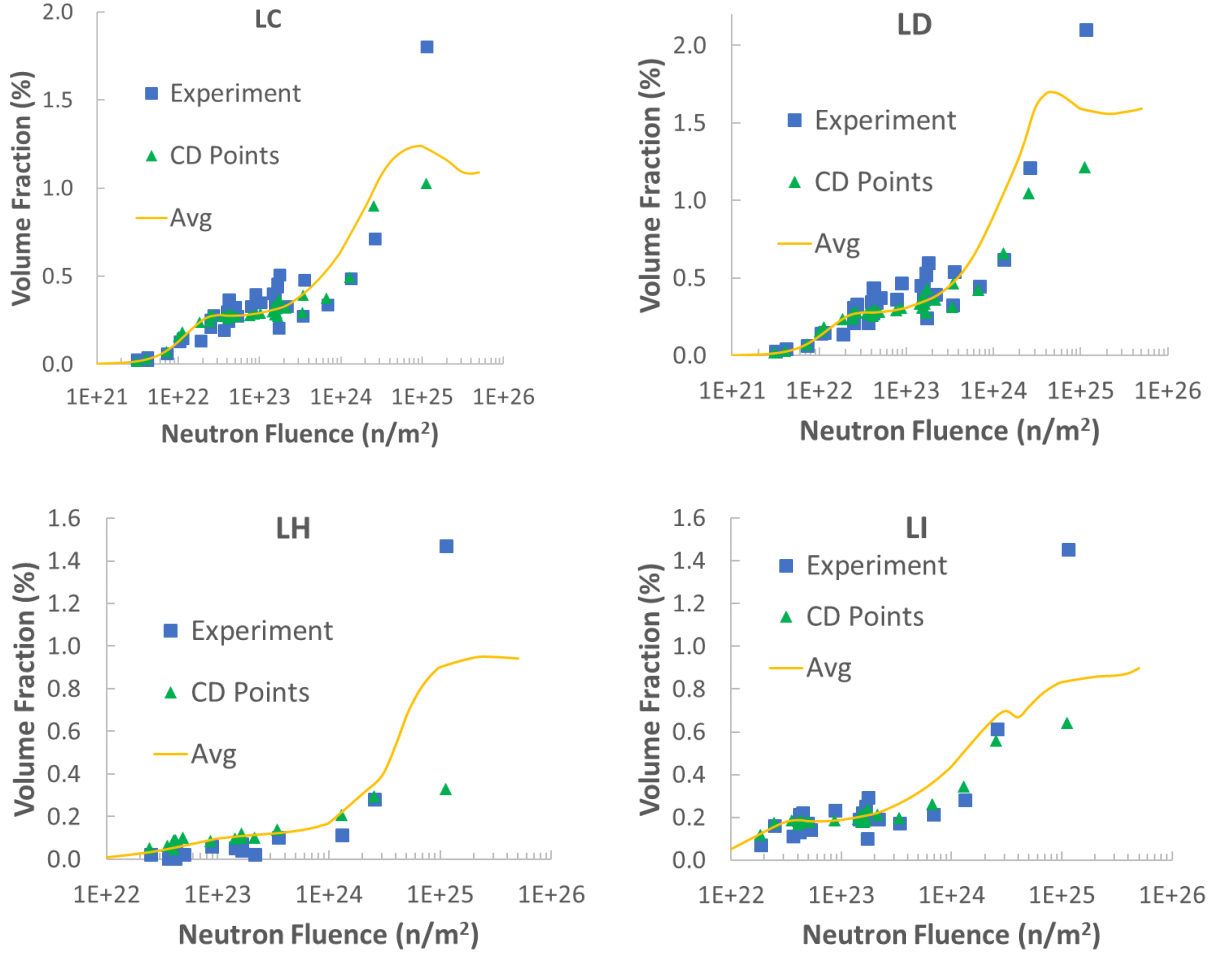


Figure 11. Comparison between CD model and experimental results for evolution of precipitates in LC, LD, LH, and LI alloys as a function of fluence. Yellow line is the CD results for an average irradiation condition (1×10^{16} n/m²/s, 290 °C) obtained using the SANS fitting process. Green triangles denoted CD points that are values calculated at the exact conditions of the experiments.

As shown in Figure 11, the CD model predicts a small drop in volume fraction at very high fluences, which is unexpected. To understand this point, we plot the detailed spatial distribution of the precipitates in Figure 12. As shown in the figure, most of the Cu precipitate are on the dislocation. The T6 appendage phase are defined as the precipitates nucleated on the fast-forming Cu precipitates, thus the T6 appendage phase is also considered as on dislocations. T3/T6 on dislocation are the MNSPs not associated with Cu, but still on dislocations. We see that from 7×10^{24} n/m² to 5×10^{25} n/m², the volume fraction of precipitates on dislocations decreases, while the volume fractions of T3/T6 precipitates on dislocations increase, but at a smaller magnitude. These changes combined appear to lead to the decrease of the total precipitate

volume fraction. From a purely thermodynamics point of view, it is difficult to understand the reduced volume fraction. However, it is possible that due to the dislocation line modified Gibbs-Thomson relationship, the coarsening kinetics of precipitates on dislocations might be modified. It is easy to understand why the precipitates evolve to eventually reside on dislocations, as these are the most stable locations. However, it appears that this process occurs more quickly than in experiments in our model. This may be in part due to the fact that our Cu diffusion coefficient likely unphysically high to compensate the fact that we ignore the mobility of small Cu clusters (described in the previous report). The high Cu diffusion may lead to faster kinetics in the simulations, leading to faster microstructural evolution compared to experiment, which result in all Cu precipitates being on dislocations. More work is needed to assess if these high-fluence processes will be altered by an improved Cu model and to what extent they might be a sign that additional physics is needed in the model.

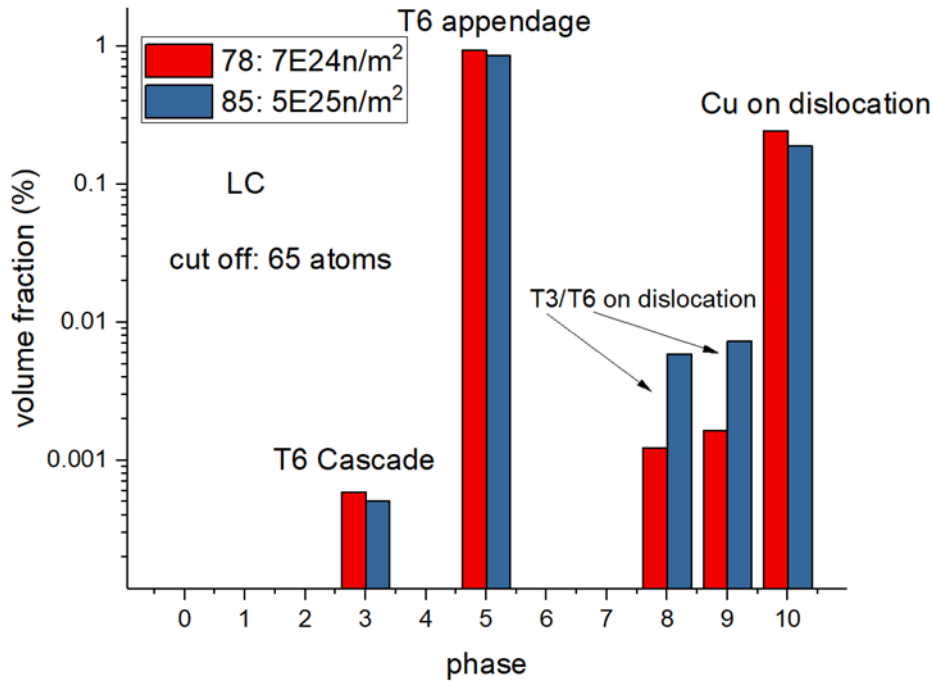


Figure 12. A detailed examination of volume fraction of different phases nucleated by various mechanisms of LC (modeled as $\text{Cu}_{0.25}\text{Ni}_{0.81}\text{Mn}_{1.1}\text{Si}_{0.46}$) alloy irradiated at a flux of $1 \times 10^{16} \text{ n m}^{-2} \text{ s}^{-1}$. The results show that at very high fluence, the volume fraction of appendage precipitates decreases, in favor of MnNiSi precipitates on dislocations.

4.2 Machine Learning

4.2.1 Results

Figure 13a shows a full fit RMSE of 15 MPa for training the model on the complete set of IVAR+ experimental data and then predicting the data back according to the input. Figure 13b shows results of best and worst fits for 5-fold CV, with an average 5-fold CV RMSE of 17.8 +/- 0.3 MPa averaged over 100 tests. The similarity in fully fitted RMSE and CV RMSE shows that the model is not prone to over-fitting. These encouraging results show that the model is robust for predicting within the IVAR+ data.

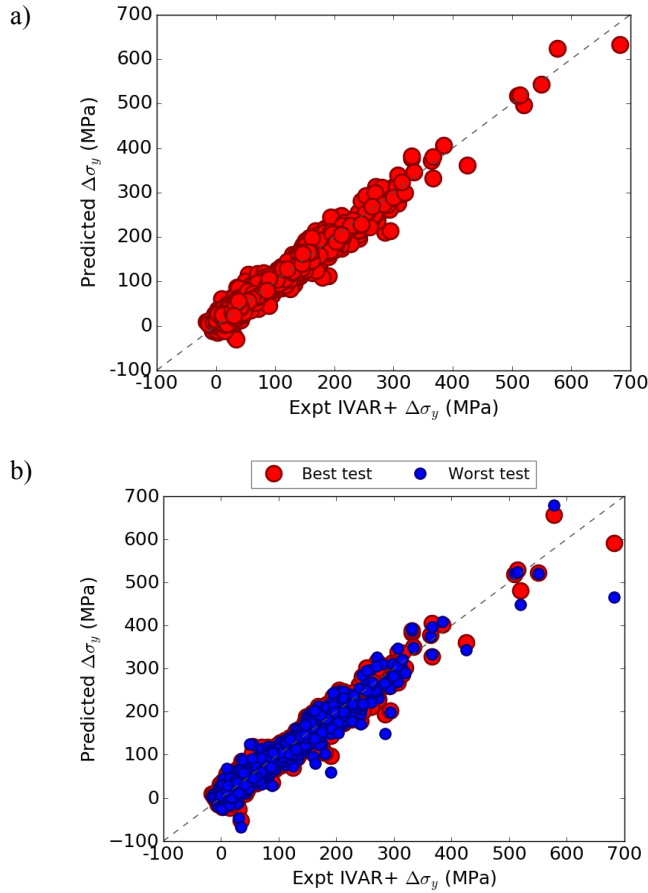


Figure 13. (a) Full fitting and (b) 5-fold cross-validation (CV) of IVAR+ experimental data using the GKRR model. The best and worst CV fits are evaluated out of 100 cross-validation tests. For each cross-validation test, the RMSE values from each of the five folds are averaged into a single RMSE value. The best CV fit has the lowest fold-average RMSE of the 100 tests, and the worst CV fit has the highest fold-average RMSE. The points shown in red or blue are for all five folds of each test.

Figure 14 shows cross validation RMSE values across a range of model hyperparameters for the IVAR+ data. Cross Validation (CV) tests like in Figure 13b are done for a range of hyperparameters α and γ and the log of the Root Mean Squared Error (RMSE) of the predictions are given in each box. Identified in orange boxes is an area of degenerate performance in which the CV test predicts the model will have very similar performance. To further test the predictive capability across this region eight models were made (scanning from top to bottom across the region) and used to predict a separate ATR2 dataset. The results are shown in Figure 15.

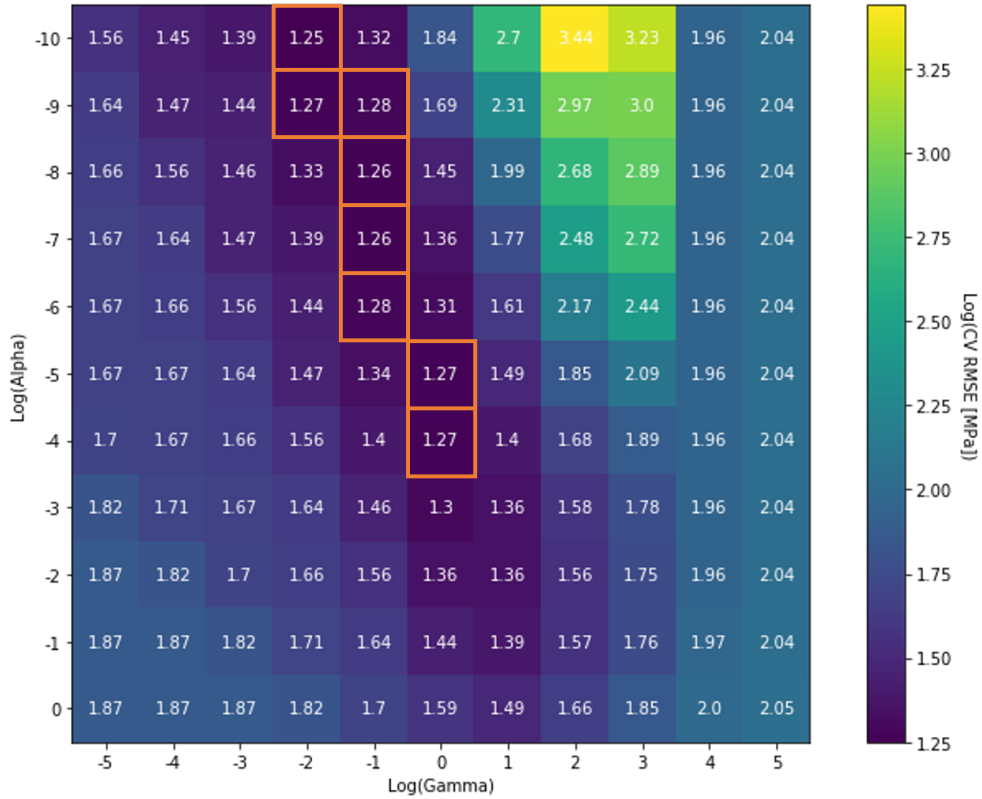


Figure 14. Heatmap of GKRR model performance across a wide range of hyperparameters. Orange boxes identify a region of degenerate performance in the hyperparameters don't significantly change the performance of the 5-fold cross validation test.

Figure 15 shows how the GKRR model performs in predicting the ATR2 dataset across the identified degenerate performance space in Figure 14. Although some combinations of hyperparameters perform similarly, there are cases where the error increases by more than 400%. This result reveals that although the cross-validation testing within the IVAR+ dataset predicts a nearly degenerate region of optimal model performance the models in this region are not equally accurate at predicting entirely new datasets such as the ATR2 dataset. Therefore, it is necessary to

find a better approach than 5-fold CV to estimate model predictive ability when trying to optimize hyperparameters for models that will be used to predict entirely new data not highly similar to IVAR+ samples.

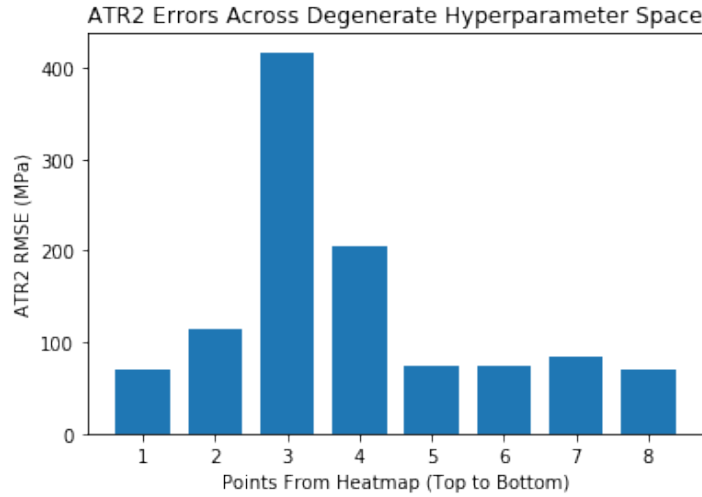


Figure 15. RMSE of predicting ATR2 dataset with 8 different hyperparameter combinations identified from the IVAR+ CV testing

To try to overcome the limitations of the GKRR model a new type of machine learning model called a Gaussian Process (GP) model was employed. The GP model functions in some ways similarly to the GKRR model, however it has different hyperparameters which could help us determine a unique model with optimal predictive ability for new data. As mentioned in the methods section, two of the three hyperparameters can be set to constant values based on the structure of our data. The third can be optimized using a grid search during the model fitting process. This means that the previous method of hyperparameter fitting using 5-fold CV can be made much faster as there is only 1 hyper parameter to optimize over. Figure 16 shows an example of the ATR2 data predicted using the GP model. The current performance is similar to the performance obtained from the best of the GKRR predictions from Figure 15 with an RMSE of around 80 MPa. It can be seen that there is still room for improvement as the model has an overall strong underprediction. In this initial test we set the GP kernel to match as closely with the previous GKRR model as possible. In the future we will explore different kernels, and optimizations of those to improve model performance and prediction.

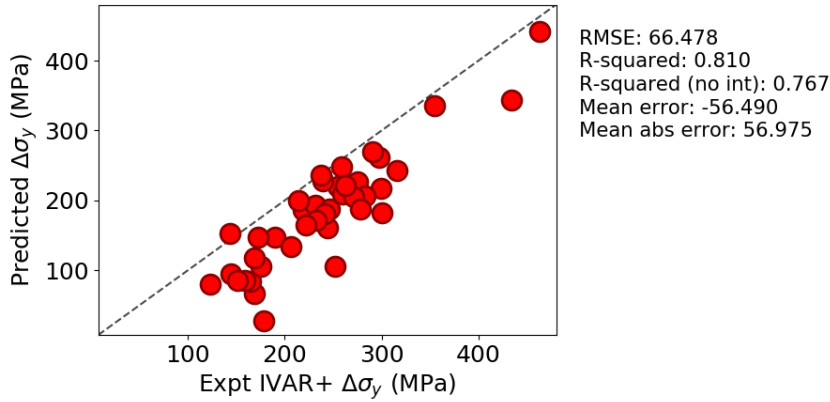


Figure 16. Gaussian Process Model prediction of the ATR2 dataset

4.3 Precipitation in Fe-Cu and Fe-Cu-Mn alloys

4.3.1 APT analysis

All of the ion irradiations resulted in significant precipitation of Cu in both the Fe-Cu and Fe-Cu-Mn alloys. Figure 17 shows four 20 nm thick atom map sections for the Fe-Cu alloy at different doses and dose rates. The longer dimension of the sections is parallel to the z-axis of the atom probe tip. Note that some of the Cu precipitates appear to be elliptical, elongating along the z-direction, which is a result of the lower evaporation field of Cu compared to the Fe matrix [53]. However, with the solute-counting based method that we used to calculate the precipitate size, the geometry of the reconstructed precipitates does not affect the results. The average precipitate sizes, number densities and volume fractions are summarized in Table 7. The volume fractions of the precipitates being similar, at 0.71 ± 0.05 at.% for all the irradiation conditions, together with the fact that the Cu concentration in the matrix being near zero suggests that the Cu precipitation is basically complete even at the lowest dose level. The precipitate sizes and number densities are also very similar for all four irradiation conditions.

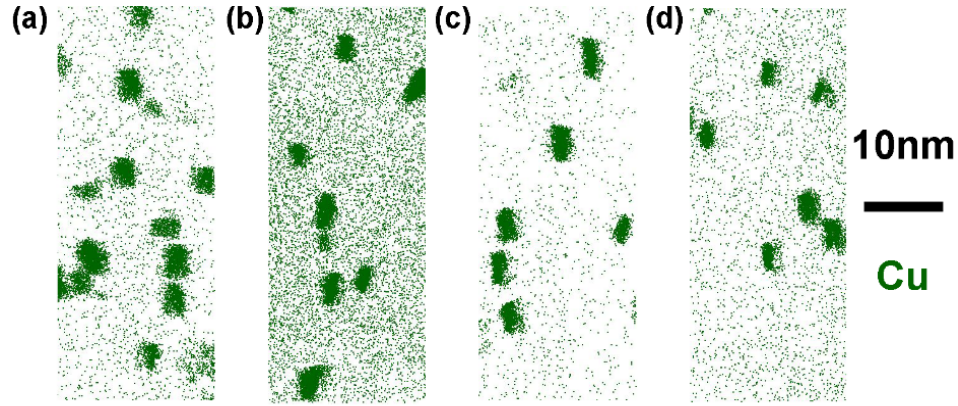


Figure 17: 20 nm thick sections from atom maps showing species distribution for Fe-Cu alloys irradiated at different doses. (a) 0.03 dpa (b) 0.3 dpa (c) 1.1 dpa (d) 3.0 dpa. Cu atoms are shown in green. Only solute atoms are shown. Note the background signal is not corrected by IVAS in the visualization of the reconstruction, which leads to higher apparent Cu composition in the matrix in some cases (for instance in the 0.3 dpa sample).

Table 7. Summary of the microstructural measurements by APT for Fe-Cu alloy

Dose (dpa)	Dose rate (dpa/s)	d (nm)	N (m^{-3})	f_v (at.%)	Cu in matrix (at.%)
0.03	3.2×10^{-7}	3.59	2.86×10^{23}	0.67	0.02 ± 0.00
0.3	3.2×10^{-6}	3.55	3.26×10^{23}	0.76	0.01 ± 0.01
1.1	1.2×10^{-5}	3.61	2.83×10^{23}	0.69	0.02 ± 0.00
3.0	3.2×10^{-5}	3.51	3.29×10^{23}	0.73	0.04 ± 0.04

Corresponding 20 nm thick atom map sections for the Fe-Cu-Mn alloy are shown in Figure 18. The precipitate size, number density, and volume fraction are summarized in Table 8. In the ternary alloy, similar to the binary case, nearly complete Cu precipitation is observed even at the lowest dpa level. However, in the ternary alloy the total volume fraction of precipitates does not saturate, but continues to increase with increasing doses. This is due to Mn enrichment in the Cu-rich core, especially at the precipitate-matrix interface, as will be shown later.

The average precipitate sizes are smaller, and the number densities are higher in the Fe-Cu-Mn alloy compared to the Fe-Cu alloy. The precipitate sizes increase slightly in the ternary alloy from 0.03 dpa to 0.3 dpa, but decrease at higher dose, although the differences are not large. In contrast, number densities increase monotonously with dose, roughly doubling between 0.03 and 3 dpa. Figure 18a illustrates the observation that the precipitates in the lowest-dose (0.03 dpa) condition tend to form in strings, indicating preferential nucleation and growth on dislocations. However, for all other irradiation conditions, the spatial distribution of the precipitates is rather uniform. The unusually high dislocation density in the lowest-dose tips (at a 300nm depth) is likely due to the polishing procedure prior to irradiation that induces some mechanical deformation immediately below the sample surface.

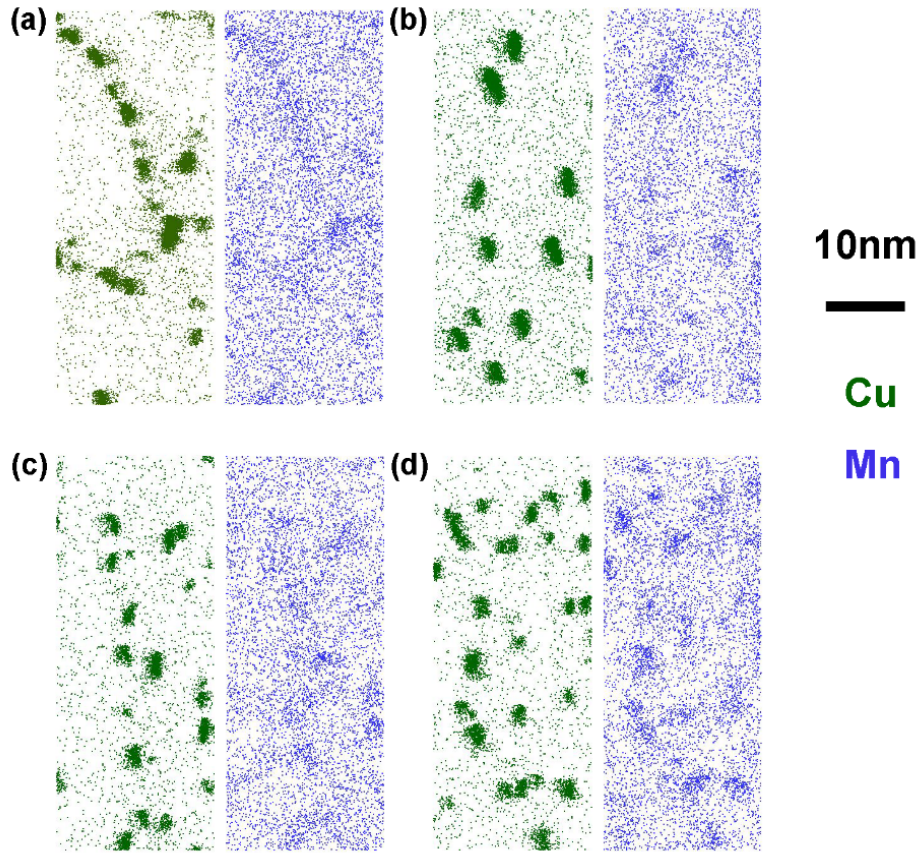


Figure 18: 20 nm thick sections from atom maps showing species distribution for Fe-Cu-Mn alloys irradiated at different doses. (a) 0.03 dpa (b) 0.3 dpa (c) 1.1 dpa (d) 3.0 dpa. Cu atoms are shown in green, and Mn atoms are shown in blue. Only solute atoms are shown.

Table 8 Summary of the microstructural measurements by APT for Fe-Cu-Mn alloy

Dose (dpa)	Dose rate (dpa/s)	d (nm)	N (m ⁻³)	f_v (at.%)	Cu in matrix (at.%)	Mn in matrix (at.%)
0.03	3.2×10^{-7}	2.70	6.28×10^{23}	0.73	0.06 ± 0.03	0.67 ± 0.02
0.3	3.2×10^{-6}	2.83	6.64×10^{23}	0.77	0.07 ± 0.01	0.60 ± 0.00
1.1	1.2×10^{-5}	2.57	9.76×10^{23}	0.88	0.01 ± 0.01	0.56 ± 0.01
3.0	3.2×10^{-5}	2.33	1.66×10^{24}	1.10	0.02 ± 0.02	0.76 ± 0.02

Figure 19 shows the size distribution of precipitates in both Fe-Cu and Fe-Cu-Mn alloys after irradiation at the four dpa values. At the lowest dose both alloys show signs of multimodal size distributions, and are broader than distributions at higher dpa. As noted previously, the precipitation in the lowest-dose sample could be affected by polishing induced dislocations. Irradiations at higher dpa levels lead to size distributions that are almost identical for Fe-Cu samples, while for the Fe-Cu-Mn alloy, the peak positions of the distributions shift to smaller sizes with simultaneously increasing dose and dose rate, and the distribution become narrower.

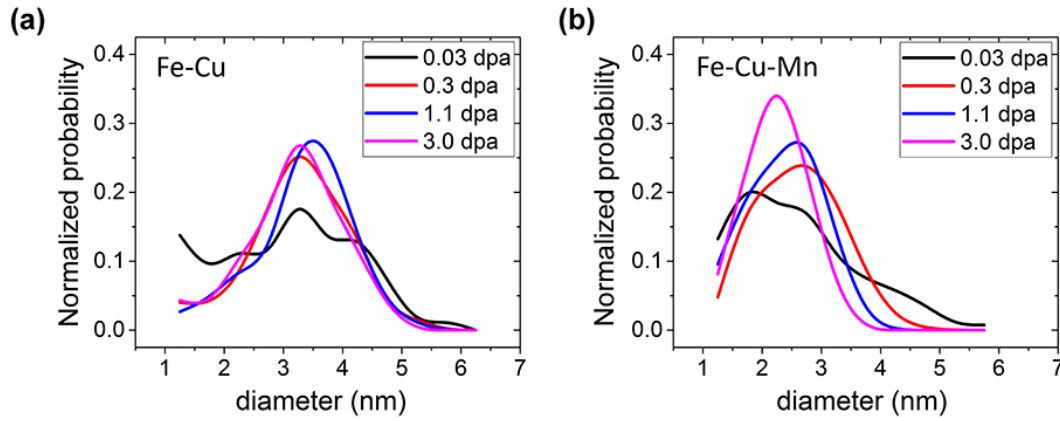


Figure 19: Precipitate size distribution. (a) Fe-Cu (b) Fe-Cu-Mn

Figure 20 shows that the fraction of Cu in Fe-Cu-Mn alloy precipitates monotonically decreases with increasing dose due to a growing Mn content. Figure 7 shows corresponding proximity histograms (proxigrams) of the Mn composition as a function of the distance from the precipitate-Fe interface. A proxigram for an Fe-Cu-Mn alloy thermally annealed at 300°C for 8300h is shown for comparison. In all cases the Mn is primarily enriched in a shell surrounding a Cu-rich core. The irradiated alloys are much more enriched in Mn, and the enrichment increases with higher dpa.

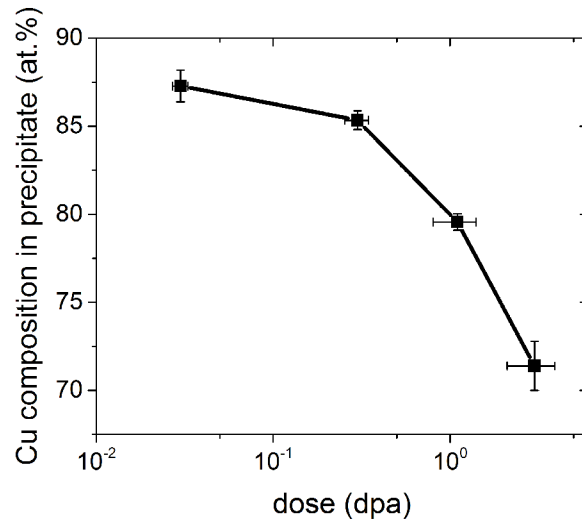


Figure 20: Cu composition in precipitates in Fe-Cu-Mn alloy as a function of irradiation dose.

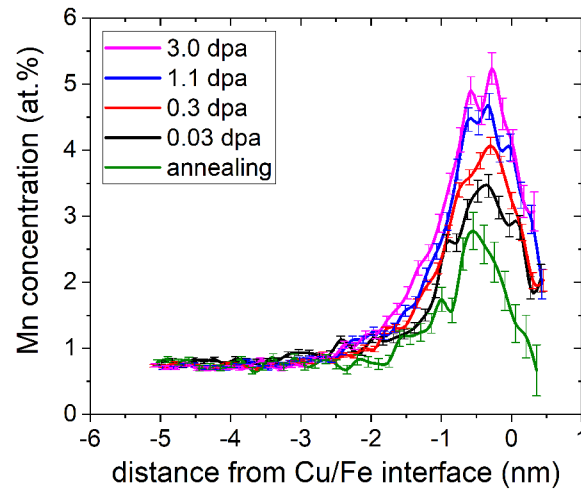


Figure 21: Radial Mn concentration profile plotted as a function of distance from Cu/Fe interface in the Fe-Cu-Mn alloy. The profiles are not corrected for Fe in the precipitates, although this Fe content is likely an artifact of the APT method.

4.3.2 Comparing results from ion irradiations and those from neutron irradiations

The same Fe-Cu and Fe-Cu-Mn alloys were previously irradiated by neutrons in test reactor, with much lower dose rates and a dpa range whose maximal value is just below that of the lowest ion irradiation dpa value. The precipitation process was characterized using the small-angle neutron scattering (SANS) technique. Details on the SANS measurements can be found in Ref.

[43]. Here we take the results from neutron irradiation experiments and compare the precipitate characteristics with those obtained in this study from ion irradiation experiments. The results are plotted a function of irradiation dose, as shown in Figure 22. The neutron results, at lower dpa levels, are plotted in red filled circles on the left side of the dashed line, while the ion results, at higher dpa levels, are plotted as filled black squares on the right side of the dashed line.

Under neutron irradiation, the precipitates in both alloys rapidly nucleate and undergo growth and coarsening, with increasing size and volume fraction, accompanied by a decreasing number density. The precipitates in the Fe-Cu-Mn alloy are far smaller and more numerous than those in the Fe-Cu binary. In contrast to the neutron irradiation trends, there is little change in the size, number density and volume fraction of the precipitates in the Fe-Cu alloy under ion irradiation. Further, while the ion irradiation volume fraction is saturated at a value close to the highest neutron dpa condition, as well as the total Cu content of the Fe-Cu alloy, the corresponding precipitate size and number densities are much smaller and larger, respectively.

The effects of ion irradiations on precipitation in the Fe-Cu-Mn alloy is very different from those in the Fe-Cu alloy. First, for the ternary alloy, the precipitate sizes and number densities are similar for the ion and neutron irradiations at a comparable dpa level (the highest for neutrons and lowest for ions). Further, it is again evident that Cu is fully precipitated at all the ion irradiation dpa levels.

In the higher-dose neutron irradiated conditions and essentially all ion-irradiation conditions, Cu is fully precipitated in both alloys. At lower neutron dose rates, the precipitates coarsen as expected, with increasing size and decreasing number density. However, at higher ion dose rates the Fe-Cu alloys have a constant size, number density and volume fraction, indicating a significant effect of BM. An even stronger apparent BM effect is observed in the Fe-Cu-Mn alloy, where the precipitate size actually decreases slightly, while the number density increases with higher dose

rates and dose. The corresponding increase in volume fraction is largely associated with an increase in the Mn content of the precipitates. It is important to point out that the interpretation of the data is confounded by correlated differences in the dose rate and dose; that is, higher dose rates are associated with higher dose. Thus, it is not possible to directly determine if the system is in a true dose rate dependent steady state (patterning regime), which is predicted by theoretical considerations.

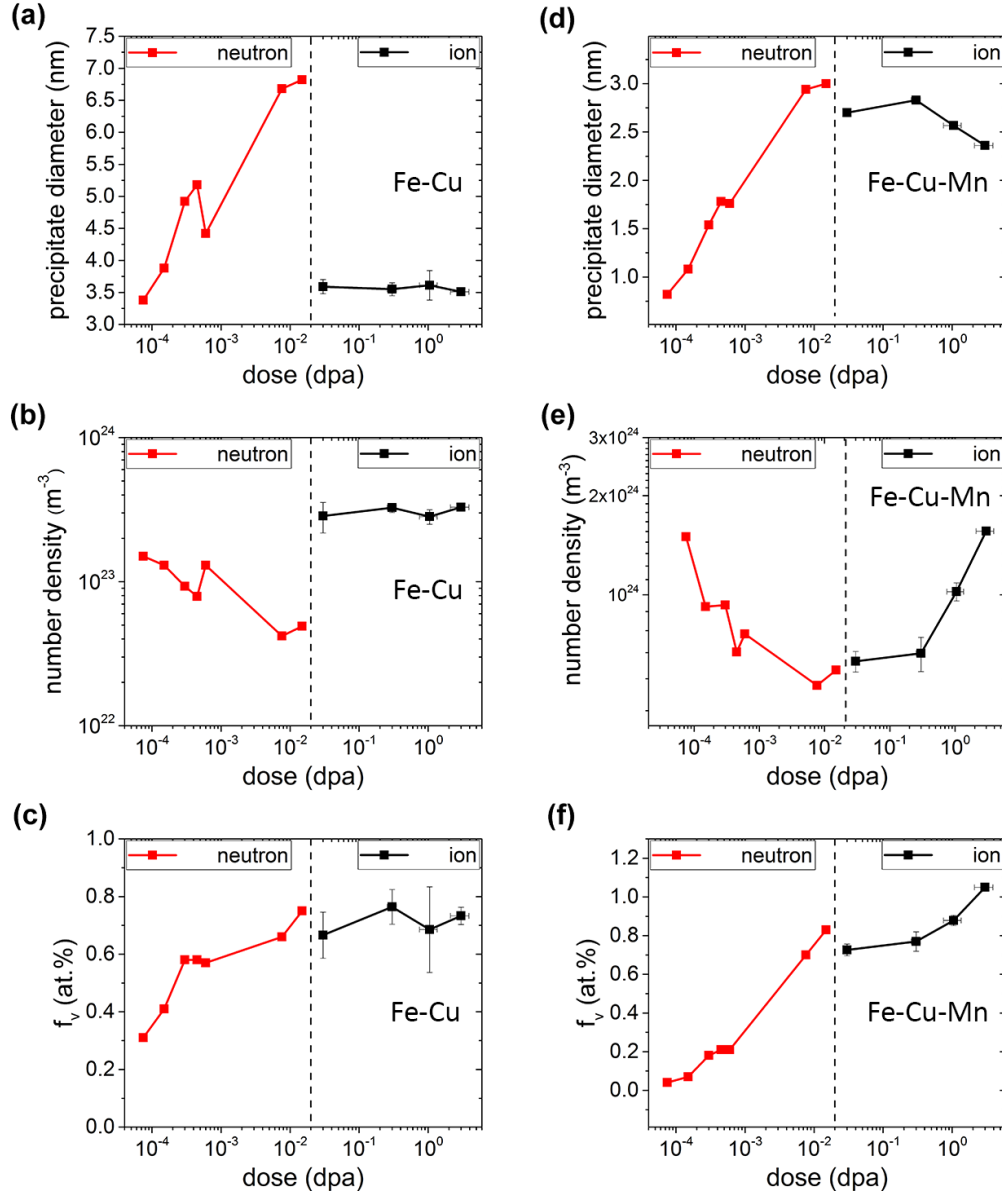


Figure 22: The precipitate volume fraction, diameter and number density of precipitates for both the Fe-Cu and Fe-Cu-Mn alloys, plotted as a function of irradiation dose.

4.3.3 Discussions

The major objective of this work is to investigate the effects of irradiation dose rate on precipitation in Fe-Cu and Fe-Cu-Mn model alloys. We have shown that precipitation in the ion-irradiated, higher-dose conditions is not a simple continuation of that in the neutron-irradiated, lower-dose case. Key observations include:

1. In the neutron-irradiated Fe-Cu alloy, the precipitate nucleation, with overlapping growth and coarsening kinetics, is similar to that expected for classical thermal diffusion-controlled kinetics, but greatly accelerated by RED. However, under ion irradiation, the precipitates are much smaller and more numerous, and do not evolve with increasing dpa.
2. In the neutron-irradiated Fe-Cu-Mn alloy, the precipitate evolution is similar to that in the Fe-Cu alloy, but the sizes are smaller and number densities are larger. However, the Fe-Cu-Mn alloy appears to experience “inverse coarsening” under ion irradiation.

We will rationalize these observations by considering the combined effects of RED and BM and the effects of Mn alloying.

As stated in the Introduction Section, the radiation enhanced diffusion coefficient D^{RED} is a complex function of a number of factors, including the fraction of mobile point defects that escapes recombination and annihilates at sinks (g_s), which is in turn determined by irradiation dose rate and sink density. With a fixed sink density, higher irradiation dose rate results in higher fraction of mobile point defects to annihilate by recombination, leading to lower D^{RED} . Therefore, for the same total irradiation dose, different dose rates can lead to different amounts of diffusion (diffusion length). Thus, to isolate the irradiation dose rate dependent RED from other dose rate effects, it is important to compare results with the same amount of diffusion, which is achieved by using the concept of effective dose (or effective dpa). As will be discussed in the following paragraph, examining results in an effective dose scale accounts for the effects of different dose rates on diffusion.

As Odette and co-workers described previously [12], the effective dpa is defined by scaling the actual irradiation dpa as

$$\text{effective dpa} = \text{dpa} \times \left(\frac{g_s(\phi)}{g_s(\phi_r)} \right),$$

where $g_s(\phi)$ and $g_s(\phi_r)$ are the fraction of vacancies that are not eliminated by recombination at the actual flux and a reference flux, respectively. Here the reference flux ϕ_r is taken as $3 \times 10^{11} \text{ n cm}^{-2} \text{ s}^{-1}$. Specifically, for ion-irradiated conditions, the irradiation dose (in unit of dpa) is first converted to an equivalent neutron fluence using the dpa cross section, then to effective dose (effective dpa). This scaling ensures that at the same effective dose, the amount of RED is the same for different irradiation conditions.

Figure 23 shows the precipitate size as a function of effective dose in unit of dpa for both model alloys. It is shown that after the scaling, the ranges of the effective dose of the ion-irradiated conditions and the neutron-irradiated conditions overlap. This suggests that although the ion irradiations result in higher irradiation doses compared to the neutron irradiations, the amounts of diffusion (effective dpa) are comparable. If the only significant dose rate effect is on RED, the curves of the ion and the neutron results are expected to collapse to one, as illustrated in Ref. [12], where all the irradiation dose rates involved are similar, and relatively low. The fact that the two curves deviate from each other indicates that other than RED, there exists other important dose rate effects, among which the BM is the most likely one. With proper combination of irradiation parameters, the BM can prevent the formation of large precipitates [54, 55]. As pointed out by Enrique and co-workers [56], when the effect of RED and BM are comparable, the system chooses a mesoscale phase separation length scale, i.e., a steady-state precipitate size in our dilute alloys. For ion-irradiated Fe-Cu and Fe-Cu-Mn samples irradiated to more than 0.3 dpa (or 0.018 and 0.0036 effective dpa, for the binary and ternary alloy, respectively), the fact that the precipitate size does not increase as a function of effective dpa suggests that the precipitates could be approaching the steady-state sizes corresponding to the particular dose rates, as predicted by the

theory [51, 56]. Such precipitate size evolution is consistent with the patterning regime. On the other hand, in neutron-irradiated conditions, the results suggest that the BM effect is not as significant as in the ion-irradiated conditions, and the precipitates grow and coarsen in a similar manner as in a thermally annealed system (while being accelerated by RED), which demonstrates macroscopic phase separation [51, 56].

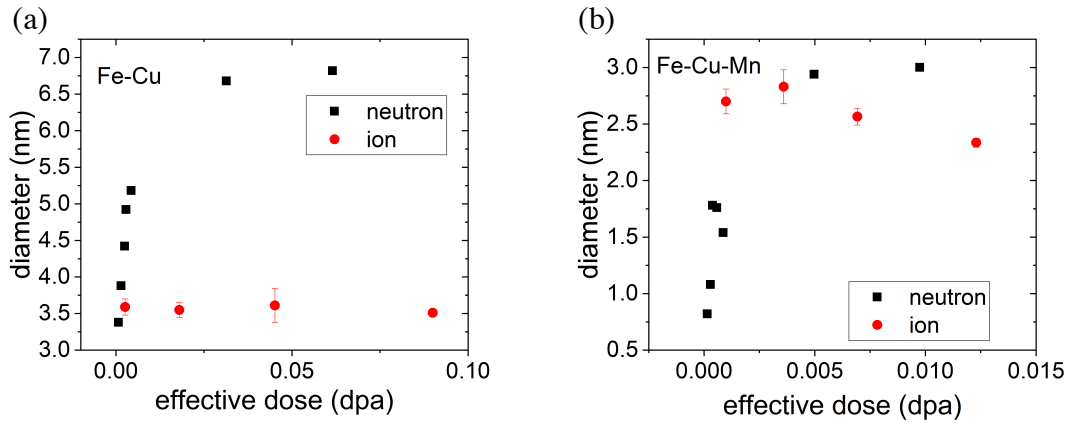


Figure 23: Precipitation size plotted as a function of effective dose (dpa), which considers the dose rate effect on RED. (a) Fe-Cu; (b) Fe-Cu-Mn.

Considering the competing effects of RED and ballistic mixing, as described in the introduction section and in Ref. [56], the relative rate of irradiation-induced ballistic jumps and radiation enhanced diffusion determines the precipitation evolution. The ballistic jump frequency of atoms relates to the dissolution rate of the precipitates by BM, while the RED coefficient characterizes the rate of bringing back solutes to the precipitates from the matrix. The important variable that determines the size of the Cu precipitate is reduced forcing parameter $\gamma = \Gamma_b / D^{\text{RED}}$. Since for neutron and heavy-ion irradiations, Γ_b is simply proportional to the point defect generation rate, the γ is determined by the dose rate dependence of D^{RED} , as will be discussed next.

The radiation enhanced diffusion coefficient of Cu can be approximately calculated as the transport of Cu via the interstitial dumbbell mechanism is not significant [57]. The thermal diffusivity of Cu [6] is readily available in the literature, thus the main task is to calculate g_s (or

equivalently C_v since $g_s = \frac{D_v C_v S_t^*}{\eta \phi \sigma_{dpa}}$, and the other values in this equation are known). To calculate g_s , we consider the production, recombination, and sink elimination of point defects in an irradiated alloy. In addition, for the Fe-Cu-Mn alloy, due to significant solubility of Mn in Fe and the relatively high vacancy-Mn binding energy, it is likely that the vacancy trapping by Mn solutes can affect the vacancy concentration significantly. Taking all these mechanisms into account, the rate theory equations can be written as

$$\begin{cases} \frac{\partial C_v}{\partial t} = \eta K_0 + \frac{C_{iv}}{\tau_t} - \frac{4\pi r_{iv}}{\Omega} (D_i + D_v) C_i C_v - D_v C_v S_t^* - \frac{4\pi r_t}{\Omega} D_v C_v C_t \\ \frac{\partial C_i}{\partial t} = \eta K_0 - \frac{4\pi r_{iv}}{\Omega} (D_i + D_v) C_i C_v - D_i C_i S_t^* - \frac{4\pi r_t}{\Omega} D_i C_i C_{iv} \end{cases}.$$

where C_v and C_i are the concentration of vacancy and interstitials; D_v ($1.14 \times 10^{-16} \text{m}^2 \text{s}^{-1}$) [12] and D_i (when solving the equation, the absolute value of D_i is not important, since D_i is much larger than D_v) are the diffusion coefficients of vacancy and interstitial; η (≈ 0.3) is the fraction of residual vacancies and SIA that escape the initial in-cascade recombination; K_0 is the production rate of point defects in unit of displacements per atom per second, dpa/s (first calculated within the NRT model [58] using SRIM [42], then corrected by the fraction of freely migrating defects [59]); C_{iv} is the concentration of occupied vacancy traps; τ_t is the average vacancy trapping time; Ω ($1.18 \times 10^{-29} \text{m}^3$) is the atomic volume of bcc Fe; S_t^* is the total sink strength of the sinks in the material; r_{iv} (0.57 nm) and r_t (0.57 nm) are the recombination and trap capture radii; C_t ($\sim 0.65\%$) is the total concentration of vacancy traps, which is taken to be the average Mn concentration in the matrix as measured by APT for each irradiation condition. The average trapping time τ_t can be calculated by [12]

$$\tau_t \approx \frac{b^2}{D_v \exp\left(-\frac{H_b}{RT}\right)} ,$$

where b (0.248 nm) is the atomic spacing, H_b is the vacancy-trap binding energy, here taken as the vacancy-Mn binding energy, which is set to 27 kJ/mol [60]. The sinks being considered are permanent sinks and temporary sinks created in cascades during irradiation, i.e., the UMF sinks, which are believed to be solute-vacancy cluster complex [12, 61-63]. The total sink strength can be written as the sum of two parts, one from permanent sinks, the other from UMFs, $S_t^* = S_t + S_{UMF}$. Permanent sinks in the calculation are modeled as pre-existing dislocations, which annihilate point defects by climbing. The pre-existing dislocation density in the two model alloys is considered to be low, and a value of $S_t = 1 \times 10^{13} \text{m}^{-2}$ is taken. Under continuous irradiation, the steady-state concentration of UMFs is approximately proportional to K_0 , but saturates at high dose rates, due to volume exclusion effects [63, 64]. The creation cross section of the UMF is taken to be $\sigma_c = 1.5 \times 10^{-29} \text{m}^2$, giving a creation rate of $\frac{\phi \sigma_c \tau_c}{\Omega}$, where τ_c is the UMF annealing time ($3 \times 10^{15} \text{s}$ at 290 °C) [12]. The UMF saturation number density is set to 10^{24}m^{-3} [63]. Taking advantage of the steady-state relationship $\frac{\partial C_v}{\partial t} = \frac{\partial C_i}{\partial t} = 0$ and $D_i C_i = D_v C_v$ [65], we can numerically solve for g_s and the associated RED as a function of K_0 (or equivalently irradiation dose rate).

The calculated RED coefficient for both Fe-Cu and Fe-Cu-Mn alloys are plotted in Figure 24a. First observation is that, at the same irradiation flux, the Cu diffusion coefficient in the Fe-Cu alloy is higher than that in the Fe-Cu-Mn alloy, which is a direct result of the vacancy trapping effects from Mn in solid solution. Second, the dose rate dependences of the Cu diffusion coefficients are different. Different from the two classical diffusion regimes (sink-elimination regime and recombination regime) that are identified in a pure metal [66], for the Fe-Cu alloy, five diffusion regimes can be identified based on the dose rate dependence. At very low dose rate, the defect

generation rate is low, and most of the point defects generated annihilate by going to the sinks. This sink-elimination regime is characterized by $D^{RED} \propto K_0$. As dose rate increases, the higher defect production rate increases the fraction of point defects that annihilate by mutual recombination, while the sink strength of the steady-state UMF sinks is comparable to the permanent sinks. In this regime, $D^{RED} \propto \sqrt{K_0}$. If the dose rate further increases, the number density of the steady-state UMF sinks increases, and eventually become the dominate sinks. In this regime, again most of the irradiation induced point defects go to the sinks. However, since the UMF concentration itself is proportional to K_0 , the resulting D^{RED} has no dependence on the dose rate, leading to a flat part of the D^{RED} curve. We name this regime the UMF-sink-elimination regime to distinguish from the (permanent) sink-elimination regime. As we previously pointed out, the UMF concentration cannot increase indefinitely, but will saturate due to the volume exclusion effect [63]. Once the UMF concentration saturates, there is no longer strong dose rate dependence of the sink strength. Thus, the system returns to the sink-elimination regime (with saturated UMF sinks), again characterized by $D^{RED} \propto K_0$. At last, at even higher dose rate, mutual recombination of the point defects again dominates, leading to $D^{RED} \propto \sqrt{K_0}$. These five regimes are separated by dashed lines in a qualitative manner in Figure 24a. For the Fe-Cu-Mn alloy, our calculation reveals that the relationship $D^{RED} \propto \sqrt{K_0}$ prevails for all the dose rates that we considered, suggesting that mutual recombination is always the dominant mechanism for defect annihilation.

Having calculated D^{RED} , we can use the reduced forcing parameter $\gamma = F_v / D^{RED}$ (Figure 24b) to directly understand the irradiation responses observed in both the neutron and ion irradiations. First, for the neutron irradiation conditions, the γ values are small, and the system is in the macroscopic phase separation regime. Coarsening similar to that in the thermal systems occurs, but the diffusion kinetics is faster for the Fe-Cu than Fe-Cu-Mn alloy (see Figure 24a), leading to

larger precipitate sizes. Second, for the ion irradiation conditions, the γ values are larger compared to neutron-irradiated ones, and the precipitates reached steady-state sizes, suggesting that the systems are in the compositional patterning regime. Third, due to the solute trapping effect imposed by Mn, the detailed γ evolution trends are different for the two alloys. For the Fe-Cu alloy, γ has a very weak dose rate dependence in the ion dose rate range, leading to constant steady-state precipitate size, as shown in Figure 23a. However, for Fe-Cu-Mn alloy, $\gamma \propto \sqrt{K_0}$, which increases in a linear manner (in log-log scale) as dose rate increases, leading to decreasing precipitate size, as shown in Figure 23b.

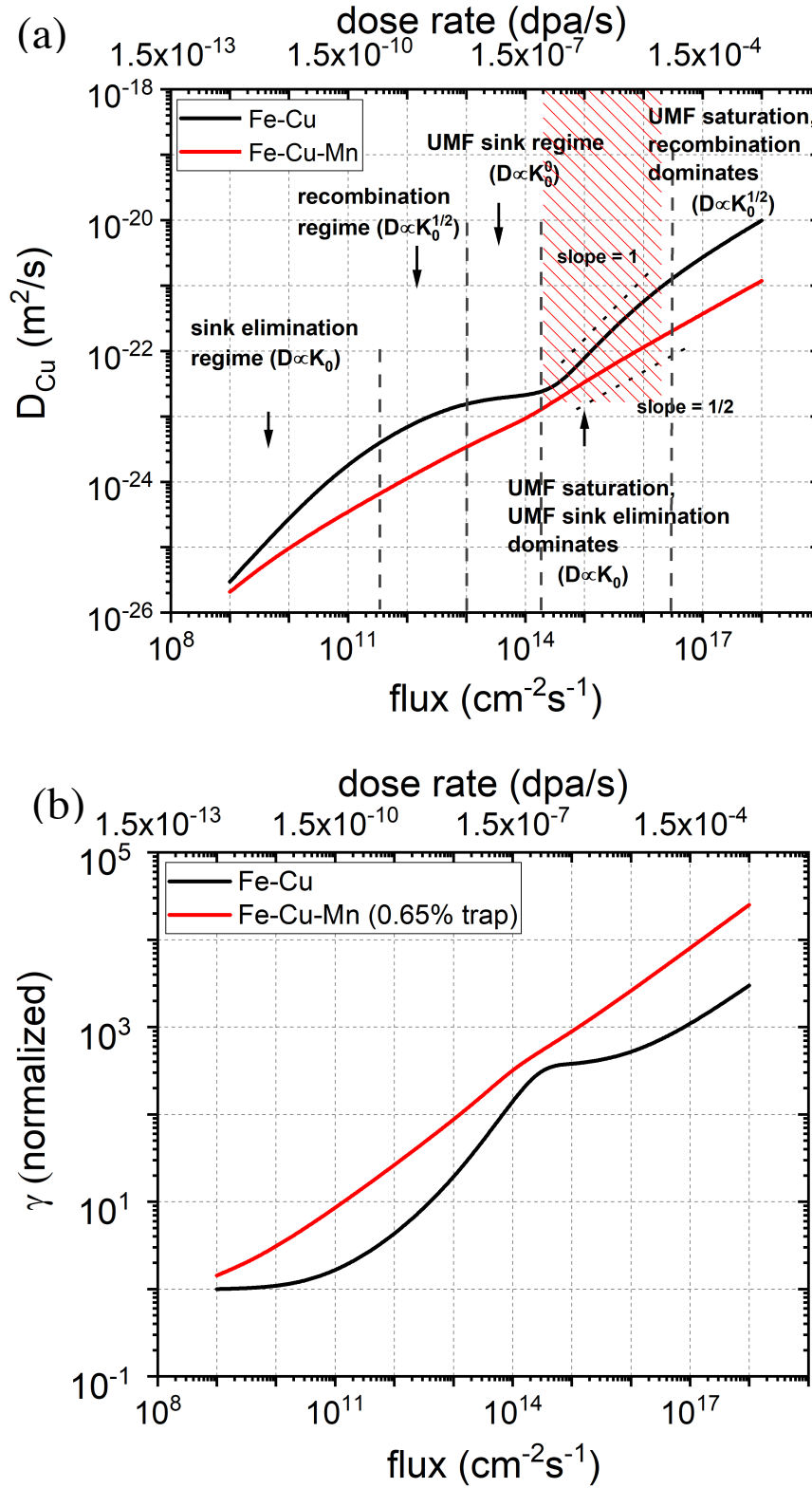


Figure 24: (a) Radiation enhanced Cu diffusion coefficient as a function of dose rate and the equivalent flux. Five diffusion regimes are denoted for the Fe-Cu alloy. (b) gamma as a function of dose rate and the equivalent flux.

5. SUMMARY OF MAJOR RESULTS

5.1 Cluster Dynamics

5.1.1 Cluster dynamics simulation of carbide precipitation in 316 stainless steel

- With the exact parameters of the current CD model at 320°C the simulation results indicate that the largest dose rate effect is on radiation enhanced diffusion, and that the ballistic mixing does not have a significant effect on the total volume fraction of the carbide phases. However, relatively minor changes in the thermodynamics associated with changes in the solute product of $\sim 4 \times$ (~ 70 meV/atom in Gibbs free energy for carbide formation), which correspond to changes expected over ~ 20 -30°C, completely change this result, leading to near total suppression of the carbide formation due to ballistic mixing, at least up to 10 dpa. Such changes are within the uncertainty of the model.
- This work suggests that the discrepancy between the expected carbide volume fraction from thermodynamics and the experimental observation of carbide volume fraction under irradiation could be due to ballistic mixing contributions, as small changes within the model uncertainty show dramatic carbide suppression from ballistic mixing. However, more work is needed for a robust prediction of ballistic mixing effects and apparent low carbide volume fractions could be due to some form of experimental error, perhaps limited sampling by the TEM method, which may miss large carbides, especially at grain boundaries.

5.1.2 Cluster dynamics simulation of Cu bearing ferritic RPV steels

- The CD model predicts a small drop in volume fraction at very high fluences, which is unexpected. Detailed analysis suggests that this drop is associated with the fact that most of the Cu precipitates, along with the associated MNS appendages, have evolved to be on dislocations. Further investigation is needed to rationalize the possible relationship between the drop in precipitate volume fraction and the microstructural evolution of precipitates to dislocations, as well as to what extent the latter is correct for real systems.

5.2 Machine Learning

- Machine learning using Gaussian Kernel Ridge Regression (GKRR) predicts the change in yield stress for compositions and conditions represented within the IVAR/IVAR+ database with a full fit and 5-fold CV RMSE of < 20 MPa.
- Predicting entirely new datasets such as the ATR2 dataset shows that 5-fold CV RMSE may not be reliable in determining hyperparameters that allow robust prediction of new datasets.
- Employing a new modeling approach, Gaussian Process Regression, can enable us to obtain robust hyperparameters and but still shows significant prediction error on new ATR2 data and needs further refinement (e.g., alternative kernels).

5.3 Precipitation in Fe-Cu and Fe-Cu-Mn alloys: dose rate effect

- We demonstrated very strong effects of irradiation dose rate on precipitation in the Fe-Cu and Fe-Cu-Mn model alloys. At the high-dose-rate of the ion irradiation, precipitates are much smaller than that under low-dose-rate neutron irradiation.
- The evolution of the sizes of the precipitates in the ion-irradiated samples is determined by competition between the radiation enhanced diffusion and irradiation induced chemical mixing. In the Fe-Cu alloy, different dominating mechanisms for point defect annihilation leads to five diffusion regimes, which are characterized by different dose rate dependence of the radiation enhanced diffusion coefficient.
- In the Fe-Cu-Mn alloy, the effect of vacancy trapping by Mn solutes significantly simplify the dose rate dependence of the diffusion coefficient, leading to only one diffusion regime for the dose rate range considered in the study.

6. FUTURE WORK

The future work is expected to focus on RPV modeling. The main focus will be in improving the CD model, including removing minor approximations we have made, identifying and fixing the source of errors in low-solute and intermediate Ni alloys, very high flux ATR1 condition simulations, and Cu diffusion, enhancing the model beyond simple p-scaling for treating radiation enhanced diffusion, and refining the model by fitting to both all the available microstructural data and to the IVAR hardening database through empirical mechanical property models. This improved model will then be further adapted and refined for modeling thermal annealing behavior to assist in mitigation efforts. We will also further refine the machine learning approach, exploring the promise of Gaussian Process Regression. The machine learning models will be tested and improved by using virtual data of hardening vs. flux, fluence, temperature and composition that include both measured conditions, e.g., like those in IVAR, and unmeasured LWR conditions. These virtual data sets will be generated by models like our CD model and can be used to test the predictive ability of the machine learning approaches.

References

- [1] A. Renault-Laborne, J. Malaplate, C. Pokor, B. Tanguy, Characterization of Precipitates in 316 Stainless Steel Neutron-Irradiated at $\sim 390^\circ\text{C}$ by the Combination of CDF-TEM, EF-TEM, and HR-TEM, Characterization of Precipitates in 316 Stainless Steel Neutron-Irradiated at $\sim 390^\circ\text{C}$ by the Combination of CDF-TEM, EF-TEM, and HR-TEM 2014.
- [2] A. Renault Laborne, P. Gavaille, J. Malaplate, C. Pokor, B. Tanguy, Correlation of radiation-induced changes in microstructure/microchemistry, density and thermo-electric power of type 304L and 316 stainless steels irradiated in the Phénix reactor, *J. Nucl. Mater.* 460 (2015) 72-81.
- [3] T. Allen, H. Tsai, J. Cole, J. Ohta, K. Dohi, H. Kusanagi, Properties of 20 % Cold-Worked 316 Stainless Steel Irradiated at Low Dose Rate, Properties of 20 % Cold-Worked 316 Stainless Steel Irradiated at Low Dose Rate 2004.
- [4] M. Mamivand, Y. Yang, J. Busby, D. Morgan, Integrated modeling of second phase precipitation in cold-worked 316 stainless steels under irradiation, *Acta Mater.* 130 (2017) 94-110.
- [5] T. Mayeshiba, H. Wu, B. Afflerbach, J. Perry, J. George, J. Cordell, G.R. Odette, D. Morgan, Machine Learning Model for Reactor Pressure Vessel Steel Embrittlement, 2018.
- [6] M. Mamivand, H.B. Ke, S. Shu, D. Morgan, G.R. Odette, P. Wells, N. Almirall, Incorporation of copper-rich precipitation model into developed Ni-Mn-Si precipitate development models, Light Water Reactor Sustainability Program, September 30, 2016 Milestone 2016.
- [7] J. Schmelzer, A new approach to nucleation theory and its application to phase formation processes in glass-forming melts, *Physics and chemistry of glasses* 45(2) (2004) 116-120.
- [8] J.W. Schmelzer, A.S. Abyzov, J. Möller, Nucleation versus spinodal decomposition in phase formation processes in multicomponent solutions, *The Journal of chemical physics* 121(14) (2004) 6900-6917.
- [9] J.W. Schmelzer, A.R. Gokhman, V.M. Fokin, Dynamics of first-order phase transitions in multicomponent systems: a new theoretical approach, *Journal of colloid and interface science* 272(1) (2004) 109-133.
- [10] V.V. Slezov, Kinetics of first-order phase transitions, John Wiley & Sons 2009.
- [11] Y. Yang, J.T. Busby, Thermodynamic modeling and kinetics simulation of precipitate phases in AISI 316 stainless steels, *J. Nucl. Mater.* 448(1) (2014) 282-293.
- [12] G.R. Odette, T. Yamamoto, D. Klingensmith, On the effect of dose rate on irradiation hardening of RPV steels, *Philos. Mag.* 85(4-7) (2005) 779-797.
- [13] H. Ke, P. Wells, P.D. Edmondson, N. Almirall, L. Barnard, G.R. Odette, D. Morgan, Thermodynamic and kinetic modeling of Mn-Ni-Si precipitates in low-Cu reactor pressure vessel steels, *Acta Mater.* 138 (2017) 10-26.
- [14] D. Xu, A. Certain, H.-J.L. Voigt, T. Allen, B.D. Wirth, Ballistic effects on the copper precipitation and re-dissolution kinetics in an ion irradiated and thermally annealed Fe-Cu alloy, *The Journal of Chemical Physics* 145(10) (2016) 104704.
- [15] A. Certain, H.J. Lee Voigt, T.R. Allen, B.D. Wirth, Investigation of cascade-induced re-resolution from nanometer sized coherent precipitates in dilute Fe-Cu alloys, *J. Nucl. Mater.* 432(1) (2013) 281-286.
- [16] C. Liu, G. Odette, B. Wirth, G. Lucas, A lattice Monte Carlo simulation of nanophase compositions and structures in irradiated pressure vessel Fe-Cu-Ni-Mn-Si steels, *Materials Science and Engineering: A* 238(1) (1997) 202-209.
- [17] P. Wells, G.R. Odette, Atom probe tomography study of CuMnNiSi precipitation in reactor pressure vessel, , Private Communication (2016).
- [18] Y. Zhang, P.C. Millett, M.R. Tonks, X.-M. Bai, S.B. Biner, Preferential Cu precipitation at extended defects in bcc Fe: An atomistic study, *Computational Materials Science* 101 (2015) 181-188.
- [19] J.W. Cahn, Nucleation on dislocations, *Acta Metallurgica* 5(3) (1957) 169-172.
- [20] D.A. Porter, K.E. Easterling, M. Sherif, Phase Transformations in Metals and Alloys, (Revised Reprint), CRC press 2009.

- [21] X. Zhang, S. Shu, P. Bellon, R.S. Averback, Precipitate stability in Cu–Ag–W system under high-temperature irradiation, *Acta Mater.* 97(0) (2015) 348-356.
- [22] K. Nohara, K. Hirano, Diffusion of Mn(54) in iron and iron-manganese alloys, *International Conference on Science and Technology of Iron and Steels*, The Iron and Steel Institute of Japan, 1971, p. 1267.
- [23] K. Hirano, M. Cohen, B.L. Averbach, Diffusion of nickel into iron, *Acta Materialia* 9(5) (1961) 440-445.
- [24] R.J. Borg, Diffusion in α -Fe-Si Alloys, *Journal of Applied Physics* 41(13) (1970) 5193.
- [25] D.W. James, G.M. Leak, Self-diffusion and diffusion of cobalt in alpha and delta-iron, *Philos. Mag.* 14(130) (1966) 701-713.
- [26] F. Christien, A. Barbu, Modelling of copper precipitation in iron during thermal aging and irradiation, *Journal of Nuclear Materials* 324(2-3) (2004) 90-96.
- [27] G.R. Odette, Private Communication (2015).
- [28] G. Odette, R. Nanstad, T. Yamamoto, A physically based correlation of irradiation-induced transition temperature shifts for RPV steels, (2007).
- [29] P. Wells, Y. Wu, T. Milot, G.R. Odette, T. Yamamoto, B. Miller, Atom probe studies of the nano-scale Mn-Ni-Si precipitates for RPV steels under irradiation, Accepted by *Acta Materialia* (2014).
- [30] M.K. Miller, M.A. Sokolov, R.K. Nanstad, K.F. Russell, APT characterization of high nickel RPV steels, *Journal of Nuclear Materials* 351(1-3) (2006) 187-196.
- [31] M.K. Miller, K.F. Russell, M.A. Sokolov, R.K. Nanstad, APT characterization of irradiated high nickel RPV steels, *Journal of Nuclear Materials* 361(2-3) (2007) 248-261.
- [32] M.K. Miller, K.F. Russell, Embrittlement of RPV steels: An atom probe tomography perspective, *J. Nucl. Mater.* 371(1–3) (2007) 145-160.
- [33] K. Fujii, K. Fukuya, N. Nakata, K. Hono, Y. Nagai, M. Hasegawa, Hardening and microstructural evolution in A533B steels under high-dose electron irradiation, *Journal of Nuclear Materials* 340(2-3) (2005) 247-258.
- [34] P.B. Wells, T. Yamamoto, B. Miller, T. Milot, J. Cole, Y. Wu, G.R. Odette, Evolution of manganese–nickel–silicon-dominated phases in highly irradiated reactor pressure vessel steels, *Acta Mater.* 80 (2014) 205-219.
- [35] G.R. Odette, Modeling of Irradiation Embrittlement in Pressure Vessel Steels, *Irradiation Effects on Pressure Vessel Steels*, IAEA IRRWG-LMNPP98-3, International Atomic Energy Agency, Vienna, Austria, 1998, p. 438.
- [36] N. Castin, L. Malerba, R. Chaouadi, Prediction of radiation induced hardening of reactor pressure vessel steels using artificial neural networks, *Journal of Nuclear Materials* 408 (2011) 30-39.
- [37] R. Kemp, G.A. Cottrell, H.K.D.H. Bhadeshia, G.R. Odette, T. Yamamoto, H. Kishimoto, Neural-network analysis of irradiation hardening in low-activation steels, *Journal of Nuclear Materials* 348 (2006) 311-328.
- [38] E.D. Eason, G.R. Odette, R.K. Nanstad, T. Yamamoto, A physically-based correlation of irradiation-induced transition temperature shifts for RPV steels, *J. Nucl. Mater.* 433(1–3) (2013) 240-254.
- [39] Python. <https://www.python.org>, 2017).
- [40] F. Pedregosa, G. Varoquaux, A. Gramfort, V. Michel, B. Thirion, O. Grisel, M. Blondel, P. Prettenhofer, R. Weiss, V. Dubourg, J. Vanderplas, A. Passos, D. Cournapeau, M. Brucher, M. Perrot, É. Duchesnay, Scikit-learn: Machine Learning in Python, *Journal of Machine Learning Research* 12 (2011) 2825-2830.
- [41] K.P. Murphy, *Machine Learning: A Probabilistic Perspective*, MIT Press, Cambridge, Massachusetts, 2014.
- [42] J.F. Ziegler, M.D. Ziegler, J.P. Biersack, SRIM - The stopping and range of ions in matter (2010), *Nuclear Instruments & Methods in Physics Research Section B-Beam Interactions with Materials and Atoms* 268(11-12) (2010) 1818-1823.

- [43] S. Shu, B.D. Wirth, P.B. Wells, D.D. Morgan, G.R. Odette, Multi-technique characterization of the precipitates in thermally aged and neutron irradiated Fe-Cu and Fe-Cu-Mn model alloys: Atom probe tomography reconstruction implications, *Acta Mater.* 146 (2018) 237-252.
- [44] D.J. Larson, T.J. Prosa, R.M. Ulfing, B.P. Geiser, T.F. Kelly, *Local electrode atom probe tomography*, New York, US: Springer Science (2013).
- [45] M.K. Miller, *Atom probe tomography: analysis at the atomic level*, Springer Science & Business Media 2012.
- [46] L.T. Stephenson, M.P. Moody, P.V. Liddicoat, S.P. Ringer, New Techniques for the Analysis of Fine-Scaled Clustering Phenomena within Atom Probe Tomography (APT) Data, *Microsc. microanal.* 13(06) (2007) 448-463.
- [47] D. Vaumousse, A. Cerezo, P.J. Warren, A procedure for quantification of precipitate microstructures from three-dimensional atom probe data, *Ultramicroscopy* 95 (2003) 215-221.
- [48] A. Cerezo, L. Davin, Aspects of the observation of clusters in the 3-dimensional atom probe, *Surface and Interface Analysis* 39(2-3) (2007) 184-188.
- [49] N.J. Cunningham, Study of the Structure, Composition, and Stability of Yttrium-Ti-Oxygen nm-Scale Features in Nano-Structured Ferritic Alloys, University of California, Santa Barbara, Santa Barbara, Calif., 2012.
- [50] M.K. Miller, B.D. Wirth, G.R. Odette, Precipitation in neutron-irradiated Fe-Cu and Fe-Cu-Mn model alloys: a comparison of APT and SANS data, *Materials Science and Engineering: A* 353(1-2) (2003) 133-139.
- [51] S. Shu, P. Bellon, R.S. Averback, Role of point-defect sinks on irradiation-induced compositional patterning in model binary alloys, *Phys. Rev. B* 91(21) (2015) 214107.
- [52] A. Renault Laborne, C. Pokor, J. Garnier, J. Malaplate, Microstructure and Grain Boundary Chemistry Evolution in Austenitic Stainless Steels Irradiated in the Bor-60 Reactor Up to 120 dpa, 14th Int. Conf. On Environmental Degradation of Materials in Nuclear Power Systems, 2009.
- [53] T. Philippe, M. Gruber, F. Vurpillot, D. Blavette, Clustering and Local Magnification Effects in Atom Probe Tomography: A Statistical Approach, *Microsc. microanal.* 16(5) (2010) 643-648.
- [54] R.S. Nelson, D.J. Mazey, J.A. Hudson, Stability of precipitates in an irradiation environment, *J. Nucl. Mater.* 44(3) (1972) 318-330.
- [55] H.J. Frost, K.C. Russell, Recoil resolution and particle stability under irradiation, *J. Nucl. Mater.* 104(0) (1981) 1427-1432.
- [56] R.A. Enrie, P. Bellon, Compositional patterning in systems driven by competing dynamics of different length scale, *Physical Review Letters* 84(13) (2000) 2885-2888.
- [57] L. Messina, Multiscale modeling of atomic transport phenomena in ferritic steels, KTH Royal Institute of Technology, 2015.
- [58] M.J. Norgett, M.T. Robinson, I.M. Torrens, PROPOSED METHOD OF CALCULATING DISPLACEMENT DOSE-RATES, *Nucl. Eng. Des.* 33(1) (1975) 50-54.
- [59] S.M. Mao, S. Dillon, R.S. Averback, The influence of Cu-Nb interfaces on local vacancy concentrations in Cu, *Scr. Mater.* 69(1) (2013) 21-24.
- [60] T.H. Youssef, G. Grais, Determination of Mn-vacancy binding energy in alpha-iron containing 1% Mn, *Scripta Metallurgica* 9(6) (1975) 603-605.
- [61] G.R. Odette, E.V. Mader, G.E. Lucas, W.J. Phythian, C.A. English, The effect of flux on the irradiation hardening of pressure vessel steels, *Effects of Radiation on Materials: Sixteenth International Symposium*, ASTM International, 1994.
- [62] E. Mader, G.E. Lucas, G.R. Odette, The effects of metallurgical and irradiation variables on the postirradiation annealing kinetics of pressure vessel steels, *Effects of Radiation on Materials: 15th International Symposium*, ASTM International, 1992.
- [63] H. Watanabe, S. Arase, T. Yamamoto, P. Wells, T. Onishi, G.R. Odette, Hardening and microstructural evolution of A533b steels irradiated with Fe ions and electrons, *J. Nucl. Mater.* 471 (2016) 243-250.
- [64] M.J. Makin, F.J. Minter, Irradiation hardening in copper and nickel, *Acta Metallurgica* 8(10) (1960) 691-699.

- [65] G.S. Was, Fundamentals of Radiation Materials Science, 2nd ed., Springer, New York. 2017.
- [66] R. Sizmann, The effect of radiation upon diffusion in metals, J. Nucl. Mater. 69–70(0) (1978) 386-412.